

MOGLI: Model for Multiphase Gas using Multifluid hydrodynamics

Hitesh Kishore Das,¹* Max Gronke,¹ Rainer Weinberger²

¹ Max Planck Institute for Astrophysics, Garching D-85748, Germany

² Leibniz-Institut für Astrophysik Potsdam (AIP), An der Sternwarte 16, 14482 Potsdam, Germany

Draft from 6 December 2024

ABSTRACT

Multiphase gas, with hot ($\sim 10^6\text{K}$) and cold ($\sim 10^4\text{K}$) gas, is ubiquitous in astrophysical media across a wide range of scales. However, simulating multiphase gas has been a long-standing challenge, due to the large separation between the size of cold gas structures and the scales at which such gas impacts the evolution of associated systems. In this study, we introduce a new subgrid framework for such multiphase gas, **MOGLI**: Model for Multiphase Gas using Multifluid hydrodynamics, in multifluid **AREPO**. We develop this approach based on first principles and theoretical results from previous studies with resolved small-scale simulations, leading to a minimal number of free parameters in the formulation. We divide the interactions in the model into three sources: drag, turbulent mixing and cold gas growth. As part of the model, we also include two methods for estimating the local turbulent velocities, one using the Kolmogorov scaling, and the other using the local velocity gradients. We verify the different components of the framework through extensive comparison with benchmark single-fluid simulations across different simulation parameters, such as how resolved the cold gas is initially, the turbulent Mach number, spatial resolution, and random initialisation of turbulence. We test the complete scheme and a reduced version, with and without cold gas growth. We find a very good qualitative and quantitative agreement across the different simulation parameters and diagnostics for both local turbulent velocity estimation methods. We also reproduce behaviour like the cold gas survival criteria as an emergent property. We discuss the applications and possible extensions of MOGLI and demonstrate its capability by running a simulation which would be computationally prohibitive to run as a resolved single-fluid simulation.

Key words: hydrodynamics – turbulence – galaxies:haloes – galaxies:evolution – galaxies:clusters:general – methods:numerical – methods:analytical

1 INTRODUCTION

Multiphase gas dynamics is prevalent in various astrophysical media, from accretion disks to galactic outflows. There are observational (Tumlinson et al. 2017; Veilleux et al. 2020), numerical and theoretical (McKee & Ostriker 1977; Donahue & Voit 2022; Faucher-Giguère & Oh 2023) evidence for the multiphase nature of astrophysical media. The multiphase nature of the interstellar medium (ISM), circumgalactic medium (CGM) and intracluster medium (ICM) significantly affects the evolution of corresponding systems, like galaxies or galaxy clusters, via processes such as their baryon cycles or feedback processes (Veilleux et al. 2005; Péroux & Howk 2020).

Recent observations have provided crucial insights into the structure of this multiphase gas, particularly in galactic halos. Studies have constrained the size of cold gas clouds in the CGM to be $\lesssim 10$ pc (Lan & Fukugita 2017; Crighton et al. 2015; Schaye et al. 2007; Rauch et al. 1999; Chen et al. 2023). This small-scale structure exists within large halos spanning tens to hundreds of kpc in radius (Tumlinson et al. 2017), creating a significant challenge for numerical simulations attempting to resolve these disparate scales – and leading to non-convergence of cosmological simulations in the halo gas content (e.g. Hummels et al. 2019; van de Voort et al. 2021).

Many theoretical studies use small-scale idealized simulation setups to better resolve and understand the small-scale gas structure. Some studies have focused on the in-situ formation of multiphase gas from the hot ambient phase via thermal instability (Field & Field 1965; Sharma et al. 2012; Mccourt et al. 2012), and the effects of turbulence (Audit & Hennebelle 2005; Mohapatra et al. 2022), magnetic fields (Sharma et al. 2010; Ji et al. 2019), metallicity (Das et al. 2021), density perturbations (Choudhury et al. 2019), rotation (Sobacchi & Sormani 2019), cosmic rays (Butsky et al. 2020), and stratification (Mohapatra et al. 2020; Wang et al. 2023). Other studies have examined the evolution of cold gas through mixing and subsequent cooling of the mixed intermediate temperature gas, particularly through cloud-crushing simulations where cold clouds are mixed and accelerated by hot outflow winds (e.g. Armillotta et al. 2016; Kanjilal et al. 2021; Abruzzo et al. 2024; Hidalgo-Pineda et al. 2024) or cold streams flowing through a hot halo (e.g. Mandelker et al. 2020; Ledos et al. 2024).

Across these small-scale studies, it has been found that resolving length scales as small as sub-parsec is crucial for achieving convergence in even the most basic properties, such as the mass distribution across different phases (McCourt et al. 2018; Gronke & Peng Oh 2018; Gronke et al. 2022). However, accurately simulating these multiphase media in large-scale simulations, which are required to capture larger flows and draw reasonable observational conclusions, remains a significant challenge due to the wide range of

* E-mail: hitesh@mpa-garching.mpg.de

scales involved. For example, to properly resolve the observed cold gas structures within a single galactic halo would require a resolution that remains computationally infeasible even for next-generation supercomputers.

There have been many approaches in astrophysical simulations to address this challenge through ‘subgrid models’ that incorporate processes occurring below the resolution limit. Notable examples include models for unresolved turbulence (Schmidt et al. 2006; Schmidt & Federrath 2011; Scannapieco & Brüggén 2008), supernova feedback (e.g. Rosdahl et al. 2017; Martizzi et al. 2016), and star formation (e.g. Federrath & Klessen 2012). Previous studies, such as Huang et al. (2020) and Smith et al. (2024) (cf. § 6.3 for an overview of previous multiphase subgrid models), have used Eulerian-Lagrangian methods for subgrid treatment of multiphase galactic outflows, where cold gas clouds are treated as particles interacting with the surrounding hot gas. Another possible approach is an Eulerian-Eulerian method, known as the ‘multifluid’ method.

The multifluid approach has been successfully applied to multiphase flows in various terrestrial contexts, including meteorology, combustion processes, and water flows. By tracking multiple fluids on the same grid, these methods allow for explicit representation of interactions between different phases (Prosperetti & Tryggvason 2007). Recently, (Butsky et al. 2024) implemented a subgrid model with a second pressureless cold fluid for unresolved cold gas clouds. In this study, we explore a different route by using an alternative implementation of the two-fluid method in the astrophysical code AREPO (Springel 2010; Weinberger et al. 2020) by (Weinberger & Hernquist 2023) to create a subgrid model. Our approach advances the multifluid framework by allowing for arbitrary volume filling fractions of each fluid, the inclusion of physically motivated coupling terms between the phases, and a thorough testing against resolved multiphase simulations.

This paper is structured as follows. In § 2, we describe the numerical setup used to implement and validate our subgrid model, titled MOGLI. In § 3, we list and explain the ingredients that go into MOGLI before validating it in § 4 and § 5 using Kolmogorov scaling and local velocity gradients-based estimates for local turbulent velocities, respectively. We discuss these results in § 6 before we conclude in § 7. The visualisations related to this study can be found here.¹

2 NUMERICAL SETUP

We use two simulation setups: the high-resolution resolved single-fluid setup using Athena++ (Stone et al. 2020) and the analogous MOGLI simulations using multifluid AREPO (Springel 2010; Weinberger et al. 2020) framework from Weinberger & Hernquist (2023) with our new subgrid model MOGLI implemented.

2.1 Turbulent box simulations

We initialise a cubic computational domain, filled with isobaric hot gas of constant density, ρ_{hot} , at a temperature, $T_{\text{hot}} = 4 \times 10^6 \text{K}$. Subsequently, we drive turbulence in this box at the largest scale, i.e. the box size (L_{box}), using the Ornstein-Uhlenbeck (OU) process (Eswaran & Pope 1988; Schmidt et al. 2006) to reach a given turbulent velocity (v_{turb}) at steady-state. We let the turbulence driving proceed for about

$7t_{\text{eddy}}$, where $t_{\text{eddy}} = L_{\text{box}}/v_{\text{turb}}$ is the eddy-turnover timescale. For the turbulence driving, we set the correlation timescale to $\sim t_{\text{eddy}}$, the driving timescale to $0.001t_{\text{eddy}}$ and solenoidal to compressive fraction, $f_{\text{sol}} = 0.3$. Note that during the turbulence-driving of the initialisation phase, there is no radiative cooling in Athena++ runs, and only a single fluid in MOGLI runs.

At the end of the initialisation phase, we restart the simulation after introducing a dense cold gas cloud with a radius R_{cloud} , overdensity $\chi = 100$ and temperature $T_{\text{cold}} = 4 \times 10^4 \text{K}$, in the centre of the box. The introduction of cloud differs between the single-fluid Athena++ and multifluid MOGLI runs, and the details are explained in Sec. 2.2 & 2.3. During the turbulence-driving in the initialisation phase, the temperature of the hot gas increases due to turbulence heating. Hence, before introducing the cloud, we rescale the temperature of each cell by a constant factor, to get the average temperature back to T_{hot} . We also repeat this two-step process, turbulent driving and the addition of cold cloud, with different random seeds for the turbulence driving to probe the stochasticity of the results.

2.2 Resolved single-fluid

For simulations with Athena++ (Stone et al. 2020), we use the default HLLC solver with Piecewise Linear Method (PLM) on primitive variables, RK2 time integrator, adiabatic equation-of-state (EOS) and cartesian geometry. Similar to Das & Gronke (2024), we use the CIE cooling curve from Wiersma et al. (2009) at solar metallicity and implement the Townsend (2009) radiative cooling algorithm with a 40-segment power-law fit on the cooling curve for calculating the radiative losses. We stop the cooling and enforce a temperature floor at $T_{\text{floor}} = 4 \times 10^4 \text{K}$.

We include radiative cooling for one set of simulations (radiative mixing) and do not have radiative cooling for the rest (non-radiative mixing). For introducing the cold gas cloud with an overdensity of $\chi = 100$ in Athena++ simulations, we set the density within the cloud region to $\chi\rho_{\text{hot}}$ and temperature to T_{hot}/χ , while keeping the local pressure and kinetic energy unchanged. We resolve the dense cold gas cloud by at least 12 grid cells along its diameter, to have converged evolution (Gronke et al. 2022; cf. Tan et al. 2021 for comparison to detailed turbulent mixing layer simulations). We vary the cloud radius (R_{cloud}) as well as the $L_{\text{box}}/R_{\text{cloud}}$ for comparison with analogous multifluid simulations. The dashed circles show the corresponding cold gas cloud size in the simulations.

2.3 Subgrid multifluid

For MOGLI simulations with multifluid AREPO, we use the default exact hydrodynamic Riemann solver, time integration, and spatial reconstruction. The details of the multifluid framework are presented in Weinberger & Hernquist (2023). We use an adiabatic EOS for the hot fluid to allow for turbulent heating and cooling. In contrast, we use a quasi-isothermal EOS for the cold fluid, which resets the internal energy after each timestep, to emulate the temperature floor and fast cooling for cold gas in resolved single-fluid simulations. We use a different (de)refinement criterion where we assume the cell is filled with hot fluid, i.e. we refine depending on $m_{\text{refine}} = \sum_k m_k \rho_{\text{hot}}/\rho_k$, where k belongs to the set of fluids. We (de)refine the cell to match m_{refine} and a target mass resolution. This (de)refinement criterion ensures that the cells with more cold fluid are not excessively refined and refinement occurs as if we only have the hot fluid.

In a multifluid simulation, we track hot and cold gas as two different fluids. Each cell has a quantity that refers to the fraction of cell volume

¹ http://hiteshkishoredas.github.io/research/mogli_subgrid.html

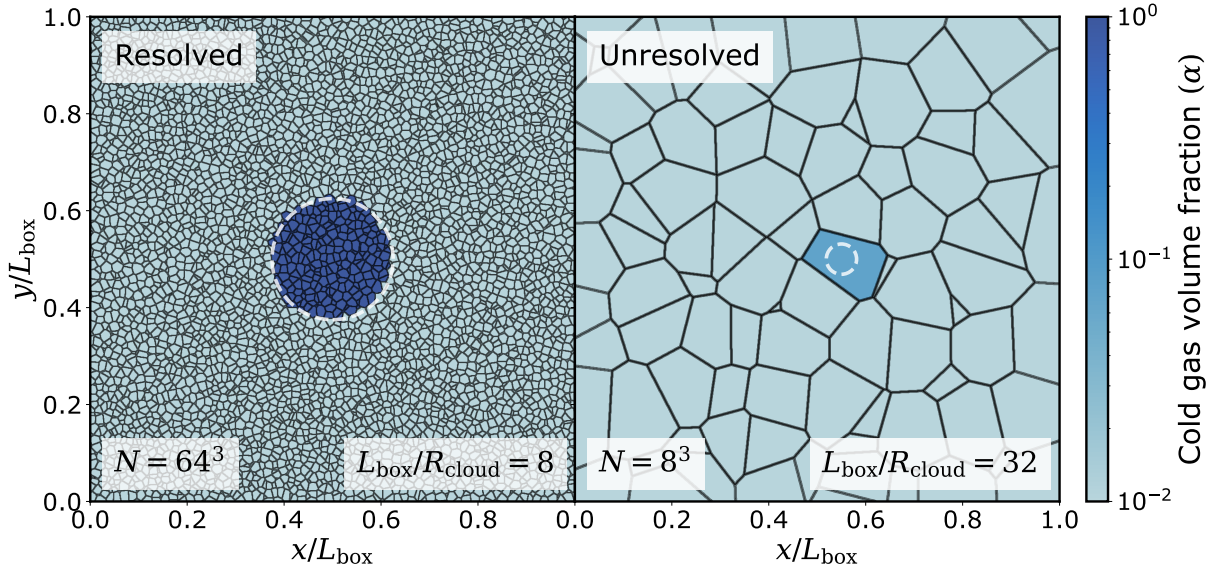


Figure 1. Initial cold fluid volume fraction slices for MOGLI simulations with resolved and unresolved cold gas clouds. The left panel shows an example of a resolved cold gas cloud with 64^3 cells and $L_{\text{box}}/R_{\text{cloud}} = 8$, where the cloud is bigger than the grid cells and grid cells inside the volume of the cloud have an $\alpha = 1 - \alpha_{\text{floor}}$. On the other hand, the right panel shows the initial cold fluid volume fraction for MOGLI simulation with an unresolved cold gas cloud, with 8^3 cells and $L_{\text{box}}/R_{\text{cloud}} = 32$. As the cold gas cloud is unresolved, the volume fraction in the cell is set to $\alpha_{\text{floor}} + V_{\text{cloud}}/V_{\text{cell}}$, where V_{cloud} and V_{cell} are the cloud and grid cell volumes. In both cases, the cells without any cold gas have a volume fraction, $\alpha = \alpha_{\text{floor}} = 10^{-8}$. The dashed circles show the corresponding cold gas cloud size in the simulations.

occupied by the fluids. As we only have two fluids in our setup, we only need to keep track of one volume fraction. We refer to the volume fraction of the cold fluid as α' and that of the hot fluid as $(1 - \alpha')$. We enforce a floor of $\alpha_{\text{floor}} = 10^{-8}$ on α' and $(1 - \alpha')$ for numerical reasons. Hence, $\alpha' = \alpha_{\text{floor}}$ for a cell filled with hot fluid and $\alpha' = 1 - \alpha_{\text{floor}}$ for one filled with cold fluid. The α_{floor} dictates the order of magnitude of the smallest amount of cold gas that can be tracked, so it has to be a sufficiently small number. We found that $\alpha_{\text{floor}} = 10^{-8}$ is small enough, and further decrease does not have a significant effect on the results, apart from the slightly higher computational costs due to stricter source integration tolerances.

After rescaling the temperature (same as the Athena++ setup; cf. Sec. 2.2 above), we take the single-fluid output at the end of the turbulence-driving in the initialisation phase and create the multifluid initial condition with the cloud. If the cloud is resolved, we fill the cells within the cloud region with cold fluid by setting $\alpha' = 1 - \alpha_{\text{floor}}$. If the cloud is not resolved, we pick the cell closest to the centre of the box and increase the α' by the amount corresponding to the volume of the unresolved cloud. If V_{cell} and V_{cloud} are the volume of the cell and the cloud, respectively, the α' is set to $\alpha_{\text{floor}} + V_{\text{cloud}}/V_{\text{cell}}$. Both fluids have the same velocity at the beginning of the simulations.

Fig. 1 shows the initial cold fluid volume fraction slices for MOGLI simulations with resolved and unresolved cold gas clouds. The left panel shows an example of a resolved cold gas cloud with 64^3 cells and $L_{\text{box}}/R_{\text{cloud}} = 8$, where the cloud is bigger than the grid cells and grid cells inside the volume of the cloud have an $\alpha = 1 - \alpha_{\text{floor}}$. On the other hand, the right panel shows the initial cold fluid volume fraction for MOGLI simulation with an unresolved cold gas cloud, with 8^3 cells and $L_{\text{box}}/R_{\text{cloud}} = 32$. As the cold gas cloud is unresolved, the volume fraction in the cell is set to $\alpha_{\text{floor}} + V_{\text{cloud}}/V_{\text{cell}}$, where V_{cloud} and V_{cell} are the cloud and grid cell volumes.

3 MOGLI: THE SUBGRID MODEL

Multifluid AREPO evolves multiple fluids on a common grid. This allows for the inclusion of terms for interactions between the fluids. In our case, the interaction terms are mass exchange (\dot{m}), momentum exchange ($\dot{\vec{p}}$) and energy exchange (\dot{E}) terms. The source terms are integrated using the Bader-Deuffhard semi-implicit integration (Bader & Deuffhard 1983; Weinberger et al., in prep). The semi-implicit integrator takes the 10 conservative variables (mass, momenta and energy for each fluid) and integrates the source functions from the subgrid model to calculate the new values over a timestep. MOGLI consists of the model for the source terms for the interactions between the hot and cold gas fluids, which we explain in this section.

3.1 Definition of the source functions

Let \mathbf{Q} and $\dot{\mathbf{Q}}$ denote the conservative variables and source functions, respectively, from the model.

$$\mathbf{Q} = \begin{bmatrix} m \\ \vec{p} \\ E \end{bmatrix}, \dot{\mathbf{Q}} = \begin{bmatrix} \dot{m} \\ \dot{\vec{p}} \\ \dot{E} \end{bmatrix} \quad (1)$$

We split the source functions into three components, that refer to contributions from three different physical processes. The first contribution, $\dot{\mathbf{Q}}_{\text{drag}}$, is due to the hydrodynamic drag between fluids. The drag interaction does not lead to a mass exchange but can result in momenta and energy exchange. The second one, $\dot{\mathbf{Q}}_{\text{mix}}$, is from the mixing between cold into hot fluid, and the third, $\dot{\mathbf{Q}}_{\text{grow}}$, is from the cooling of the mixed gas from hot fluid to cold fluid. Both second- and third-source function contributions involve mass, momenta, and energy exchange. So, the full source function can be written as

$$\dot{\mathbf{Q}} = \dot{\mathbf{Q}}_{\text{drag}} + \dot{\mathbf{Q}}_{\text{mix}} + \dot{\mathbf{Q}}_{\text{grow}}. \quad (2)$$

While mass and momentum are conserved for all the different

parts of the source functions, energy is only conserved for \dot{Q}_{drag} and \dot{Q}_{mix} . For \dot{Q}_{grow} , the energy is not conserved as thermal energy is dissipated via radiative cooling and the difference between the energy exchange is given by \dot{E}_{cooling} . We can write the conservation relations as

$$\dot{Q}_{\text{drag,cold}} = -\dot{Q}_{\text{drag,hot}}, \quad (3)$$

$$\dot{Q}_{\text{mix,cold}} = -\dot{Q}_{\text{mix,hot}}, \quad (4)$$

$$\dot{Q}_{\text{grow,cold}} = -\dot{Q}_{\text{grow,hot}} - \begin{bmatrix} 0 \\ 0 \\ \dot{E}_{\text{cooling}} \end{bmatrix}. \quad (5)$$

From here onwards, we will denote elements of the ‘cold’ or ‘hot’ source functions with $_{\text{cold}}$ or $_{\text{hot}}$, respectively.

3.2 The cold gas volume filling fraction

As volume fraction is not part of the 10 conservative variables, we need to calculate the volume fraction from the conservative quantities.

$$\alpha' = \frac{m_{\text{cold}} u_{\text{cold}}}{m_{\text{cold}} u_{\text{cold}} + m_{\text{hot}} u_{\text{hot}}} \quad (6)$$

where u_{hot} and u_{cold} are the specific internal energy of the hot and cold fluid, respectively. As α has a floor and ceiling value, we redefine the volume fraction such that values between α_{floor} and α_{ceil} map linearly to their physical values in $[0, 1]$. So, a cell filled with hot fluid and $\alpha' = \alpha_{\text{floor}}$ corresponds to $\alpha = 0$, while a cell filled with cold fluid and $\alpha' = 1 - \alpha_{\text{floor}}$ corresponds to $\alpha = 1$. This new mapped value is subsequently used for calculations in the source functions.

$$\alpha = \begin{cases} 0.0 & \text{for } \alpha' < \alpha_{\text{floor}} \\ \frac{\alpha' - \alpha_{\text{floor}}}{1 - 2\alpha_{\text{floor}}} & \text{for } \alpha \in [\alpha_{\text{floor}}, 1 - \alpha_{\text{floor}}] \\ 1.0 & \text{for } \alpha' > 1 - \alpha_{\text{floor}} \end{cases} \quad (7)$$

3.3 Drag forces

One obvious change of momentum and energy stems from the hydrodynamic drag between the fluids in a cell, in the presence of a relative velocity $\Delta\vec{v}$ giving rise to \dot{Q}_{drag} in Eq. (2). The drag force between the two fluids in the cell will be

$$\dot{p}_{\text{drag,cold}} = -\vec{F}_{\text{drag}} = 0.5 C_D \rho_{\text{hot}} A_{\text{cross}}(\alpha) |\Delta\vec{v}| \Delta\vec{v} \quad (8)$$

where $C_D = 0.5$ is the drag coefficient and $A_{\text{cross}}(\alpha)$ is the cross-sectional area of the cold fluid in the direction of the relative velocity. We further discuss the functional form of A_{cross} (Eq. (33)) in Section 3.7.

Drag force also leads to an exchange of energy between the two fluids. The rate of energy exchange is set to,

$$\dot{E}_{\text{cold}} = -\vec{F}_{\text{drag}} \cdot \vec{v}_i. \quad (9)$$

Here, \vec{v}_i is the centre of mass velocity, which will be attained at equilibrium (Saurel & Abgrall 1999), i.e.,

$$\vec{v}_i = \frac{m_{\text{cold}} \vec{v}_{\text{cold}} + m_{\text{hot}} \vec{v}_{\text{hot}}}{m_{\text{cold}} + m_{\text{hot}}} = \frac{\vec{p}_{\text{cold}} + \vec{p}_{\text{hot}}}{m_{\text{cold}} + m_{\text{hot}}}. \quad (10)$$

As mentioned earlier, the drag force contribution does not cause mass exchange. Hence, the final form of $\dot{Q}_{\text{drag,cold}}$ is

$$\dot{Q}_{\text{drag,cold}} = \begin{bmatrix} 0 \\ -\vec{F}_{\text{drag}} \\ -\vec{F}_{\text{drag}} \cdot \vec{v}_i \end{bmatrix}. \quad (11)$$

Later, in Sec. 4.1 & 5 we include \dot{Q}_{drag} and verify the MOGLI model.

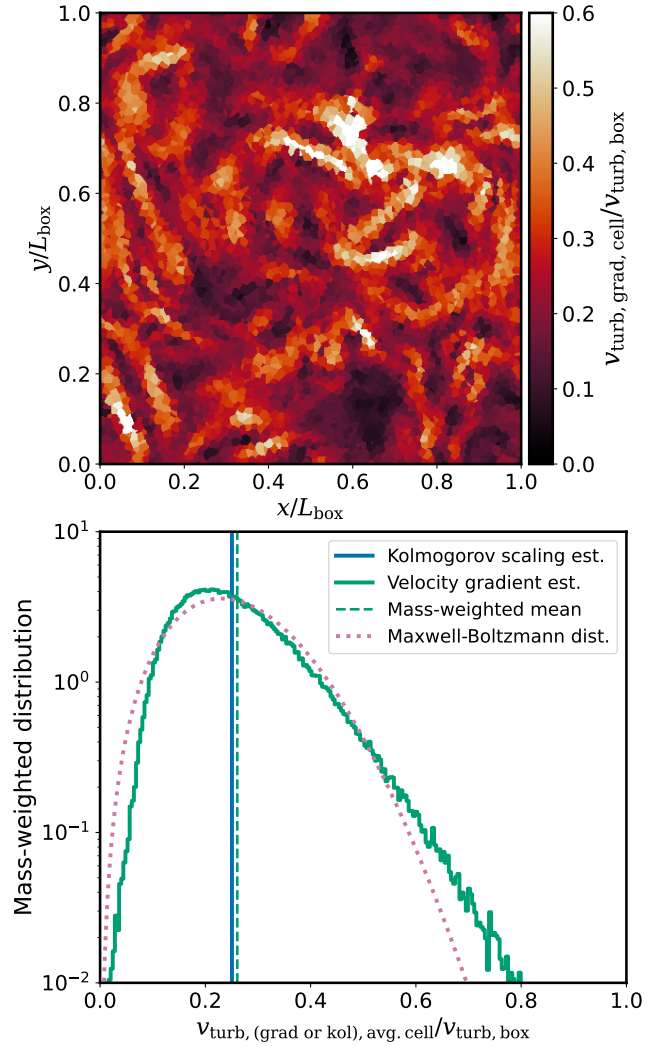


Figure 2. *Top panel* shows a slice of $v_{\text{turb,grad}}$ from a simulation with a turbulent Mach number, $M_{\text{turb,box}} = 0.5$ at the box scale. It shows how the velocity gradient-based estimation (grad) can capture the spatial variation in the local velocity dispersion, in other words, the local turbulent velocity. *Bottom panel* shows, in solid lines, the distribution of the local turbulent velocity, at the scales of average cell size instead of local cell size, in the same snapshot as the top panel. We find that while the mass-weighted mean of from grad method, shown as the dashed green line, agrees with the estimate from kol, shown as the solid blue line. The pink dotted line shows the expected Maxwell-Boltzmann distribution with the same mean as the mass-weighted mean from kol method. Even though the mean turbulent velocity from the two simulations are very similar, the distribution of velocities is drastically different, with the kol method leading to a fixed value for a fixed length scale, and the grad method matching the expected Maxwell-Boltzmann distribution.

3.4 Turbulent Mixing

Next, we consider the contribution to source functions from the turbulent mixing of cold gas into hot gas. This part of the source function contains mass, momenta and energy exchange and is captured by \dot{Q}_{mix} (cf. Eq. (2)).

To first order, we expect the turbulent mixing to destroy the cold gas on a characteristic timescale t_{destroy} , i.e., $\dot{m}_{\text{cold} \rightarrow \text{hot}} \sim m/t_{\text{destroy}}$. From previous work as well as analytical considerations, we expect

this destruction timescale to be the Kelvin-Helmholtz or Rayleigh-Taylor timescale of the cloud (e.g. Klein et al. 1994; Gronke et al. 2022)

$$t_{\text{destroy}} = \frac{\chi^{1/2} l_{\text{cold}}}{v_{\text{turb}}}. \quad (12)$$

Here, l_{cold} is the effective size of the cold gas in the cell

$$l_{\text{cold}} = \left(\frac{\alpha V_{\text{cell}}}{4\pi/3} \right)^{1/3}, \quad (13)$$

v_{turb} is the turbulent velocity, and χ overdensity of a given cell

$$\chi \equiv \frac{\rho_{\text{cold}}}{\rho_{\text{hot}}} = \left(\frac{1}{\alpha} - 1 \right) \frac{m_{\text{cold}}}{m_{\text{hot}}}. \quad (14)$$

Note that while χ is independent of α for a given cell, l_{cold} strongly depends on it and thus gives rise to a short destruction time for, e.g., a predominantly hot cell. We explicitly verified this destruction term in Sec. 4.1 & 5. While we calculate l_{cold} as the size of a monolithic cold cloud in the cell, it refers to the length-scale of the cold gas which we subsequently use to calculate destruction timescale, t_{destroy} in Eq. (12), it does not relate to the cold gas structure within the cell.

Within any cell, we expect the mass exchange to slow down and drop with increasing volume fraction of the cold fluid, due to the decrease in the interface area between the two fluids, over which the exchange can happen; for instance, we expect a cold gas cell surrounded by other gas cells with a ~ 1 cold gas volume fraction this mass exchange rate to be ~ 0 as the cell is entirely ‘shielded’ from the hot medium. We include an extra multiplicative factor, i.e. the area factor, of $2h(\alpha)$ to account for this dependence on the interface area. This factor essentially encodes the details of the subgrid cold gas structure. The exact form of this factor is derived and discussed in § 3.7².

We find that solely the area factor, $2h(\alpha)$, is inadequate to suppress the cold gas destruction in cells which have a high cold fluid mass fraction, $\alpha_{\text{mass}} = m_{\text{cold}}/(m_{\text{cold}} + m_{\text{hot}})$, especially for cases with resolved cold gas. This can be easily understood through additional ‘shielding’ as those predominantly cold gas cells are mostly also surrounded by other predominantly cold gas cells preventing their destruction. The effect is that the mass exchange from cold to hot occurs only in cells that possess a mass fraction α_{mass} less than a threshold. We find that a α_{mass} threshold of 0.15 works well across all tests (§ 4.1), i.e.,

$$\dot{m}_{\text{cold} \rightarrow \text{hot}} = \begin{cases} 2h(\alpha) \frac{m_{\text{cold}}}{t_{\text{destroy}}} & \alpha_{\text{mass}} < 0.15 \\ 0 & \text{otherwise.} \end{cases} \quad (15)$$

The momenta and energy exchange are the corresponding fluxes caused by the mass exchange. Hence, we get a source function contribution due to mixing,

$$\dot{\mathbf{Q}}_{\text{mix,cold}} = \begin{bmatrix} -\dot{m}_{\text{cold} \rightarrow \text{hot}} \\ -\vec{v}_{\text{cold}} \dot{m}_{\text{cold} \rightarrow \text{hot}} \\ -\frac{1}{2} \dot{m}_{\text{cold} \rightarrow \text{hot}} v_{\text{cold}}^2 - \dot{m}_{\text{cold} \rightarrow \text{hot}} u_{\text{cold}} \end{bmatrix} \quad (16)$$

3.5 Cold gas growth

Finally, we include the source function contribution due to the cooling of mixed gas to create more cold gas. Previous studies like Gronke et al. (2022) have shown that for cases that are well within the growth

² Note that we deliberately did not absorb the factor 2 into the fudge factor to facilitate comparison with prior work; cf. § 3.7

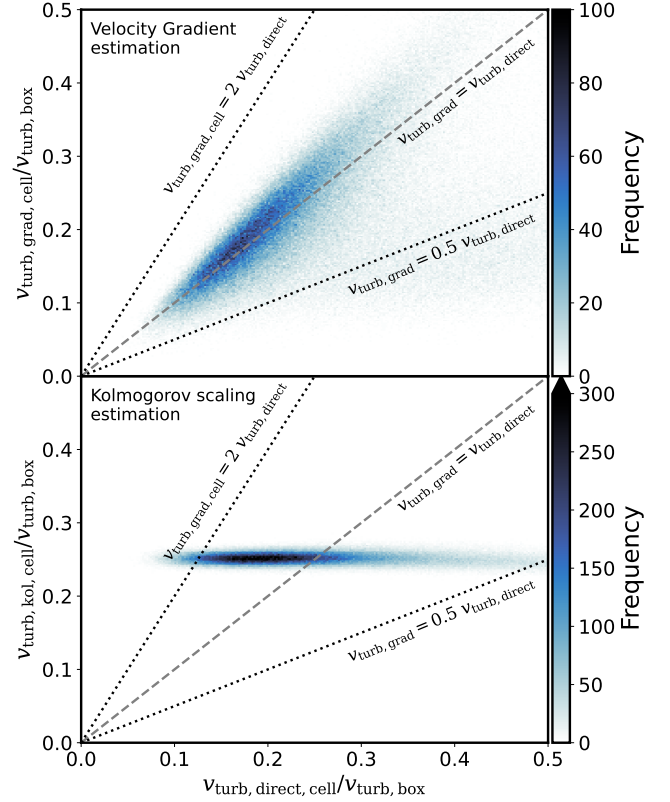


Figure 3. The comparison between the directly calculated velocity dispersion ($v_{\text{turb,direct}}$) and the approximated local velocity dispersions using both estimation methods. The top panel shows the comparison with the velocity gradient-based method (**grad**) and the bottom panel show the comparison with the Kolmogorov spectrum-based method (**kol**).

regime, the cold gas mass follows an exponential growth, with a characteristic timescale of $t_{\text{grow}} \sim \chi(t_{\text{cool,cold}}/v_{\text{turb}})^{1/2}$, i.e., characterised by the geometric mean of the cold gas mixing and cooling time, and where l refers to the cold gas structure lengthscale and v_{turb} is the turbulent velocity at the lengthscale l . Note that this growth time is backed up by analytical arguments of combustion theory and numerically verified using small-scale simulations (Tan et al. 2021). We can rewrite the expression for t_{grow} in terms of the local cell properties as,

$$t_{\text{grow}} = \chi(t_{\text{destroy}} t_{\text{cool,cold}})^{1/2} \alpha^{1/9} \quad (17)$$

where the additional factor $\alpha^{1/9}$ arises to account for the effective cold gas size within a cell.

Both t_{destroy} and $t_{\text{cool,cold}}$ can be calculated from local grid cell properties, but in our tests, we consider a fixed value of $t_{\text{cool,cold}}$. We use the value of t_{cc} and the required ratio if $t_{\text{cool,cold}}/t_{\text{cc}}$ to obtain the required value of $t_{\text{cool,cold}}$. We also include the area factor of $2h(\alpha)$ for this interaction, same as Eq. (15), which gives the hot to cold fluid mass exchange rate,

$$\dot{m}_{\text{hot} \rightarrow \text{cold}} = 2h(\alpha) \frac{m_{\text{cold}}}{t_{\text{grow}}} \quad (18)$$

As mentioned earlier, the energy across the system is not conserved during cold gas growth. The difference in internal energy during the mass exchange from hot to cold fluid is radiated away and hence

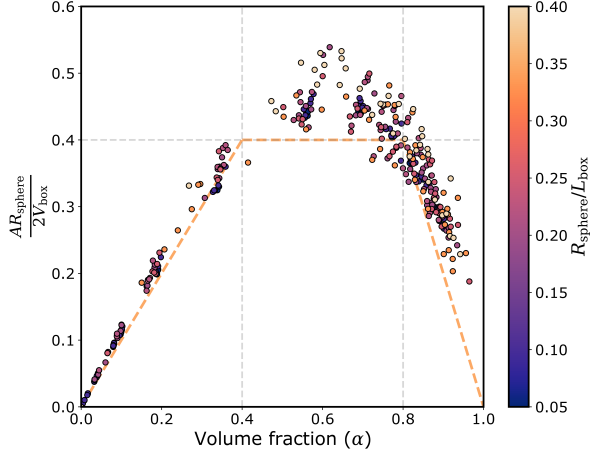


Figure 4. Variation of $AR/(2V_{\text{box}})$ with volume fraction (α) in a 3D box. The colour of the points shows the size of the individual spheres, relative to the box size and the orange lines correspond to the approximate fit for the points (Eq. (30)).

subtracted

$$\dot{E}_{\text{cooling}} = \dot{m}_{\text{hot} \rightarrow \text{cold}}(u_{\text{hot}} - u_{\text{cold}}). \quad (19)$$

Including the momentum exchange due to mass exchange, we obtain the expression for the source function contribution due to cold gas growth

$$\dot{\mathbf{Q}}_{\text{grow,cold}} = \begin{bmatrix} \dot{m}_{\text{hot} \rightarrow \text{cold}} \\ \vec{v}_{\text{hot}} \dot{m}_{\text{hot} \rightarrow \text{cold}} \\ \frac{1}{2} \dot{m}_{\text{hot} \rightarrow \text{cold}} v_{\text{hot}}^2 + \dot{m}_{\text{hot} \rightarrow \text{cold}} u_{\text{hot}} \end{bmatrix} - \begin{bmatrix} 0 \\ 0 \\ \dot{E}_{\text{cooling}} \end{bmatrix}. \quad (20)$$

3.6 Turbulent velocity estimation

Turbulence is key in mixing hot and cold material, and thus, the expressions in $\dot{\mathbf{Q}}_{\text{mix}}$ and $\dot{\mathbf{Q}}_{\text{grow}}$ depend on the local turbulent velocity at the scale of cold fluid in the cell, as $v_{\text{turb}} = v_{\text{turb,cell}}(l_{\text{cold}}/l_{\text{cell}})^{1/3}$, where l_{cell} is the cell size. The most accurate way to accomplish this is to have a turbulence model that keeps track of the subgrid turbulence (akin to Schmidt et al. 2006 or Semenov 2024). As the implementation of such a model in a moving-mesh code like AREPO is out of the scope of this study, we use two methods to approximate the turbulence at the grid cell scales.

3.6.1 Estimation by Kolmogorov Scaling (ko1)

The first method (ko1) assumes that the turbulence is fully developed and follows the Kolmogorov spectrum to the subgrid scales. So, by scaling the box-scale turbulent velocity ($v_{\text{turb,box}}$) down to the grid cell scale, we can estimate the local turbulence.

$$v_{\text{turb,ko1,cell}} = v_{\text{turb,box}} \left(\frac{l_{\text{cell}}}{L_{\text{box}}} \right)^{1/3} \quad (21)$$

This method is feasible for setups with fully developed turbulence at a resolved scale, like our turbulent box simulations. However, it is not appropriate in simulations with significant spatial and/or temporal variation in turbulence.

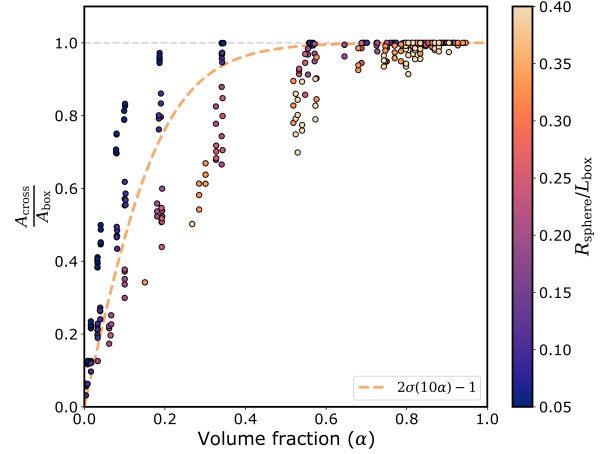


Figure 5. Variation of A/A_{box} with volume fraction (α) in a 3D box. The colour of the points shows the size of the individual spheres, relative to the box size and the orange lines correspond to the approximate fit for the points (Eq. (33)).

3.6.2 Estimation by velocity gradients (grad)

The second method of local turbulence estimation (**grad**) avoids the problems of the ko1 method by estimating the local velocity dispersion at any given time. We use the Jacobian of the velocity vector ($\mathbf{J}_{ij} = \partial v_i / \partial x_j$), to estimate velocity dispersion at the grid scale ($\sigma_{\vec{v},\text{cell}}$), and assume a fully-developed Kolmogorov spectrum on smaller scales to estimate the turbulent velocity at the subgrid cold gas scale (l_{cold}) from the calculated grid-scale.

As explained in Pakmor et al. (2016), in AREPO, the gradient of a quantity, say ϕ , in the i^{th} cell ($\vec{\nabla}_i \phi$) is calculated to be the best fit for Eq. (22), over all neighbouring cells. Let the i^{th} have n_{ngb} neighbouring cells, each denoted by a subscript j ,

$$\phi_j = \phi_i + \vec{\nabla}_i \phi \cdot \vec{x}_{ji}. \quad (22)$$

We use Eq. (22) to calculate the mean of ϕ over the neighbouring cells in n_{ngb} including the i^{th} cell,

$$\mu_i(\phi_j) = \phi_i + \vec{\nabla}_i \phi \cdot \mu_i(\vec{x}_{ji}). \quad (23)$$

Subsequently, we use the Eq. (23) for the mean to calculate the standard deviation for ϕ , σ_{ϕ}^2 .

$$\sigma_{\phi}^2 = \frac{1}{n_{\text{ngb}} + 1} \sum_j^{n_{\text{ngb}}} \left[\vec{\nabla}_i \phi \cdot (\vec{x}_{ji} - \mu_i(\vec{x}_{ji})) \right]^2 \quad (24)$$

To evaluate the Eq. (24) further, we need to make some assumptions. First, we assume that the neighbouring cells are uniformly distributed around the current cell. Hence, the weighted average of the displacements, $\mu_i(\vec{x}_{ji})$ is expected to have a marginal magnitude and can be ignored. Next, we assume that the neighbouring cells are at roughly equal distances of x_{ngb} from the current cell, and we can replace \vec{x}_{ji} with $x_{\text{ngb}} \hat{x}_{ji}$. Here, \hat{x}_{ji} refers to the unit vector in the direction of \vec{x}_{ji} , i.e. $\hat{x}_{ji} = \vec{x}_{ji}/|\vec{x}_{ji}|$. This simplifies Eq. (24) to

$$\sigma_{\phi}^2 = \frac{x_{\text{ngb}}^2}{n_{\text{ngb}} + 1} \sum_j^{n_{\text{ngb}}} \left[\vec{\nabla}_i \phi \cdot \hat{x}_{ji} \right]^2. \quad (25)$$

Eq. (25) shows that the velocity dispersion is related to the root-mean-square value of the component of gradient towards the neighbouring cells. The exact value of this quantity will depend on the relative position and number of the neighbouring cells. Hence, to further simplify the Eq. (25), we postulate that this value is close to the value at the limit of $n_{\text{ngb}} \rightarrow \infty$, with all the neighbouring cells uniformly distributed around the current cell. This allows us to rewrite Eq. (25) in its integral form and to obtain the value at the limit by evaluating the integral,

$$\sigma_{\phi, n_{\text{ngb}} \rightarrow \infty} = \sqrt{\frac{1}{3}} x_{\text{ngb}} |\nabla_i \phi| \quad (26)$$

To replace ϕ with v_x, v_y and v_z ³ in Eq. (26), we use the approximation $x_{\text{ngb}} \approx V_{\text{cell}}^{1/3}$. This yields an estimate of the local turbulence

$$v_{\text{turb,grad,cell}} = (\sigma_{v_x}^2 + \sigma_{v_y}^2 + \sigma_{v_z}^2)^{1/2} = V_{\text{cell}}^{1/3} \sqrt{\frac{1}{\xi} \sum_{i,j}^3 \left(\frac{\partial v_j}{\partial x_i} \right)^2} \quad (27)$$

where, $\xi = 3$. For multifluid simulations, if there are n_k fluids, we evaluate the local turbulent velocity with Eq. (27) for each fluid separately and take the mass-weighted average as the final turbulent velocity estimate per cell, i.e.,

$$v_{\text{turb,grad,cell}} = \frac{1}{m_{\text{cell}}} \sum_k^{n_k} m_k v_{\text{turb,grad,k}} \quad (28)$$

3.6.3 Comparison and validation of the methods

The top panel of Fig. 2 shows a slice of $v_{\text{turb,grad,cell}}$ from a simulation with a turbulent Mach number, $\mathcal{M}_{\text{turb,box}} = 0.5$ at the box scale using $N_{\text{cells}} = 64^3$ resolution elements. It shows how the velocity gradient-based estimation (grad) can capture the spatial variation in the local velocity dispersion, in other words, the local turbulent velocity. The bottom panel shows, in solid lines, the estimation for local turbulent velocity at the lengthscale of the average cell size ($l_{\text{cell,avg}} = (V_{\text{box}}/N_{\text{cell}})^{1/3}$) in the same snapshot as the top panel. As the `kol` only depends on the lengthscale, it returns a fixed local turbulent velocity for a fixed lengthscale. The blue solid line shows the `kol` method estimate for the $l_{\text{cell,avg}}$. The green solid line shows the distribution of the grad estimates for local turbulent velocities at scale of l_{cell} , and the green dashed line shows the corresponding mass-weighted mean. We find that the estimate from `kol` and mass-weighted mean from grad agree very well with each other, and the expected value $\bar{v}_{\text{turb}} \approx v_{\text{turb,box}}/N_{\text{cells}}^{1/3}$.

As the turbulence velocities along each basis directions ($v_{\text{turb,x}}, v_{\text{turb,y}}, v_{\text{turb,z}}$) roughly follow gaussian distribution, the turbulent velocity magnitude $v_{\text{turb}} = (v_{\text{turb,y}}^2 + v_{\text{turb,y}}^2 + v_{\text{turb,z}}^2)^{1/2}$ is expected to follow a Maxwell-Boltzmann distribution. In Fig. 2, the pink dotted line shows the expected Maxwell-Boltzmann distribution, with the same mean as the the mass-weighted mean from grad method. We find that the distribution of local turbulent velocity estimate from grad matches well with the Maxwell-Boltzmann distribution, with some deviations at small and large velocity magnitudes. The deviations at small velocity magnitudes are likely due to the resolution limit and lack of small scales, while the deviations at the larger velocities are probably due to slope-limiting for the gradients.

³ Note that the velocity gradients used in the MOGLI simulations are the slope-limited gradients that are used in the finite-volume solver.

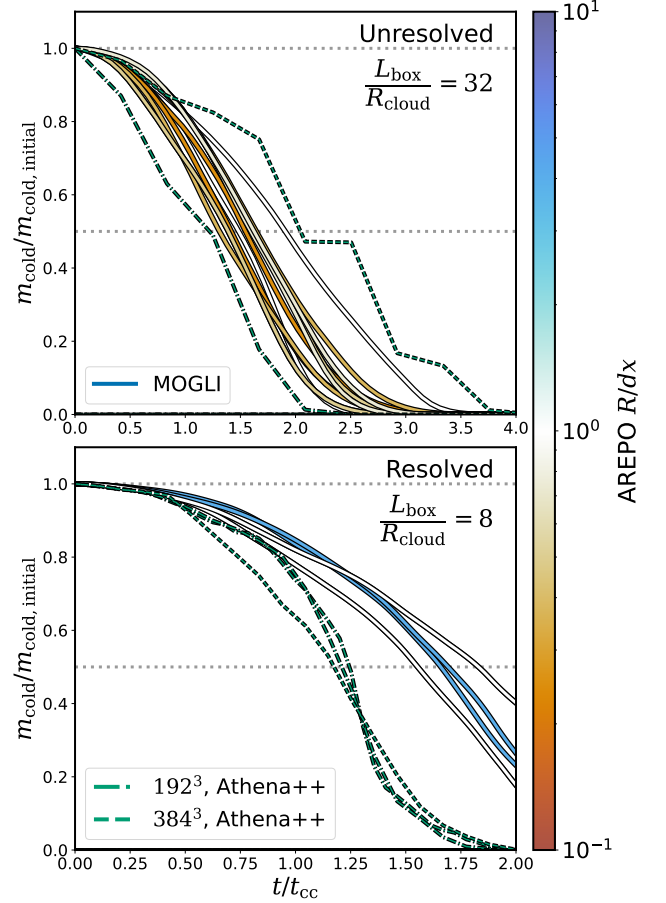


Figure 6. Cold gas evolution in non-radiative MOGLI runs with time, normalised to the initial cloud-crushing time (t_{cc}), with $\mathcal{M}_{\text{turb}} = 0.5$. The solid lines show the cold gas evolution, as the total mass of the cold fluid, with the colour of the line denoting the initial R_{cloud}/dx . The dot-dashed and dashed lines show the cold gas evolution in the benchmark Athena++ simulations, with resolutions 192^3 and 384^3 respectively. *Top panel* shows the evolution for simulations with unresolved initial cloud $L_{\text{box}}/R_{\text{cloud}} = 32$ and *bottom panel* shows the same for resolved initial cloud $L_{\text{box}}/R_{\text{cloud}} = 8$. This shows that the cloud destruction timescales in MOGLI are in agreement with the timescales in benchmark Athena++.

In order to test the ability of Eq. (28) to approximate the local velocity dispersion, we calculate the velocity dispersion at grid cell size in the neighbourhood for each grid cell in the simulation, $v_{\text{turb,direct}}$ and use it as the benchmark we want to approximate. As the directly calculated velocity dispersion is over the whole neighbourhood with a volume $V_{\text{ngb}} = \sum_{\text{ngb}} V_{\text{cell,j}}$, we use the Kolmogorov scaling to scale it down to the grid cell size as $v_{\text{turb,direct}} = \sigma_{\text{turb,ngb}} (V_{\text{cell}}/V_{\text{ngb}})^{1/9}$ where the latter term introduces corrections of order unity.

Fig. 3 shows the comparison between the directly calculated velocity dispersion ($v_{\text{turb,direct}}$) and the approximated local velocity dispersions using both estimation methods. The top panel shows the comparison with the velocity gradient-based method (grad) and the bottom panel show the comparison with the Kolmogorov spectrum-based method (`kol`). For the bulk of the cells, $v_{\text{turb,direct}}$ and $v_{\text{turb,grad}}$ agree well with each other and are within a factor of 2 between each other. The slight deviations from $v_{\text{turb,direct}}$ are likely due to the assumptions involved in obtaining the Eq. (27). On the other hand,

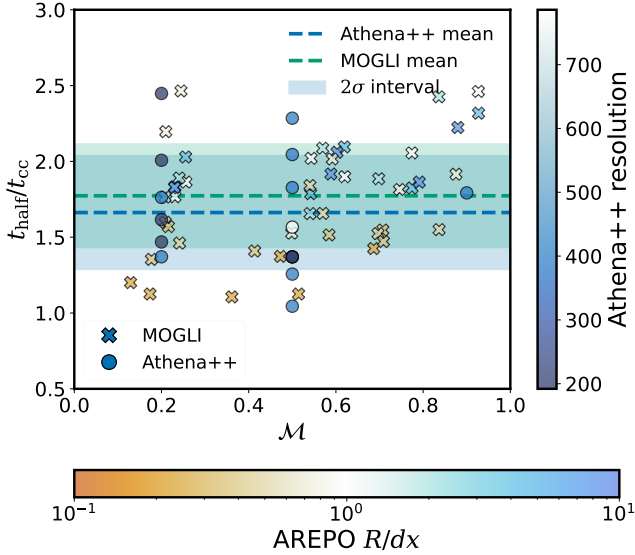


Figure 7. Scatter plot of the half mass time (t_{half}) normalised to the initial cloud-crushing timescale ($t_{\text{cc}} = \chi R_{\text{cloud}}/v_{\text{turb}}$), for different turbulent Mach numbers. Athena++ simulations with different resolutions (192^3 , 384^3 , and 768^3 , represented by the colour of the point) and turbulence random seeds to capture the inherent stochasticity of cold gas destruction in a turbulent medium.

the $v_{\text{turb,ko1}}$ from the `ko1` method is unable to capture the spatial variations in the $v_{\text{turb,direct}}$.

During our non-radiative turbulent mixing tests, explained later in Sec. 5, we find a $\xi = 2$ works better in matching with the benchmark Athena++ simulations. Hence, we use $\xi = \xi_{\text{MOGLI}} \equiv 2$ in MOGLI runs,

$$v_{\text{turb,grad,cell,MOGLI}} = V_{\text{cell}}^{1/3} \sqrt{\frac{1}{\xi_{\text{MOGLI}}} \sum_{i,j} \left(\frac{\partial v_j}{\partial x_i} \right)^2}. \quad (29)$$

Later, in Sec. 4 and 5 we test our MOGLI model with both Kolmogorov scaling-based (`ko1`) and velocity gradient-based (`grad`) methods for local turbulent velocity estimation, respectively. See Appendix A for more general version Eq. (29), which can also be applied to 2D geometries.

3.7 Cold gas surface and cross-sectional area

Both the mass exchange from hot to cold and cold to hot medium naturally depend on the exposure of the two media, and thus crucially depend on the size of the interface area in any given cell. In order to account for non-spherical and overlapping cold gas structures, we use two area factors in the model introduced in Sec. 3.4 & 3.5 (cf. Eq. (15) & (18)).

The first area factor, $2h(\alpha)$, corresponds to the dependence on the interface area between the two fluids. The second area factor, $A_{\text{cross}}(\alpha)$, is for the cross-sectional area along the relative velocity of the fluid.

We take a Monte-Carlo approach to approximate these area factors. We generate a fixed grid box with a varying number of equally sized, spheres, allowing for overlapping spheres⁴. We calculate the

⁴ We also tried different sphere size distributions but did not find any ma-

surface area (A) of the resulting ensemble of spheres using the `scikit-learn`'s marching cubes algorithm (Pedregosa et al. 2011; Lorensen & Cline 1987), and volume fraction (α) as the ratio of the volume of encapsulated cells and grid volume (V_{box}). We repeat this exercise with different radii of spheres (R_{sphere}).

We find, as shown in Fig. 4, that the quantity $AR_{\text{sphere}}/(2V_{\text{box}})$ seems to follow a general relation with the volume fraction.

$$\frac{AR_{\text{sphere}}}{2V_{\text{box}}} = \alpha h(\alpha) = \begin{cases} \alpha & \text{if } \alpha \in [0, 0.4) \\ 0.4 & \text{if } \alpha \in [0.4, 0.8) \\ 2 - 2\alpha & \text{if } \alpha \in [0.8, 1] \end{cases} \quad (30)$$

where $h(\alpha)$ is a function of volume fraction, which we define for convenience in later derivations⁵.

Assuming that the spheres are composed of cold gas, with an overdensity of χ and density of $\chi\rho_{\text{hot}}$, we obtain a relation for the interface area as a function of the volume fraction,

$$A = \frac{2h(\alpha)\alpha V_{\text{box}}}{R_{\text{sphere}}} = \frac{2h(\alpha)m_{\text{cold}}}{\chi\rho_{\text{hot}}R_{\text{sphere}}}. \quad (31)$$

Substituting the area (A) from Eq. (31) in the expression for mass exchange (e.g., Tan et al. 2021) we obtain

$$\dot{m}_{\text{cold}} = A\rho_{\text{hot}}v_{\text{flux}} = \frac{m_{\text{cold}}}{\chi R_{\text{sphere}}/v_{\text{flux}}} 2h(\alpha) = 2h(\alpha) \frac{m_{\text{cold}}}{t_{\text{flux}}} \quad (32)$$

which introduces the cold gas surface area factor of $2h(\alpha)$. Here, $t_{\text{flux}} \sim \chi R_{\text{sphere}}/v_{\text{flux}}$ is the naive mass doubling/halving time of a spherical object. Note that the factor of 2 along $h(\alpha)$ can explain the fudge factor 0.5 used in t_{grow} in (Gronke et al. 2022). At low cold gas volume fractions, Eq. (32) reduces to the empirical exponential growth rate expression observed in previous studies like (Gronke et al. 2022).

We take a similar approach to approximate the dependence of cross-sectional area in the direction of relative velocity, on the volume fraction. Assuming an isotropic distribution of the spheres, the cross-sectional area should be independent of the direction of the relative velocity. We calculate the cross-sectional area (A_{cross}) and volume fraction (α) of a varying number of randomly distributed spheres along the three axes of the grid and repeat it for different radii of the spheres (R_{sphere}). Fig. 5 shows the dependence of A_{cross} normalised to the grid's cross-sectional area, i.e. $A_{\text{box}} = L_{\text{box}}^2$, on the volume fraction of the spheres. There is a scatter, where larger individual spheres lead to a lower cross-sectional area for the same volume fraction. However, the trend converges with smaller individual clouds, and we use a sigmoid function to approximate this relation.

$$A_{\text{cross}}(\alpha) = V_{\text{cell}}^{2/3} \left(\frac{e^{10\alpha} - 1}{e^{10\alpha} + 1} \right) \quad (33)$$

With this, we have the complete and fully-defined MOGLI model and can move to verifying this model in the next section.

4 VERIFICATION: WITH KOLMOGOROV TURBULENCE ESTIMATION

As the turbulent velocity estimation is a fundamental part of the model, we verify the two estimates separately and present the results

for impact on the results while significantly increasing the number of free parameters.

⁵ We also tested similar fits to the points in Fig. 4, including higher order ones, but it does not change the results significantly.

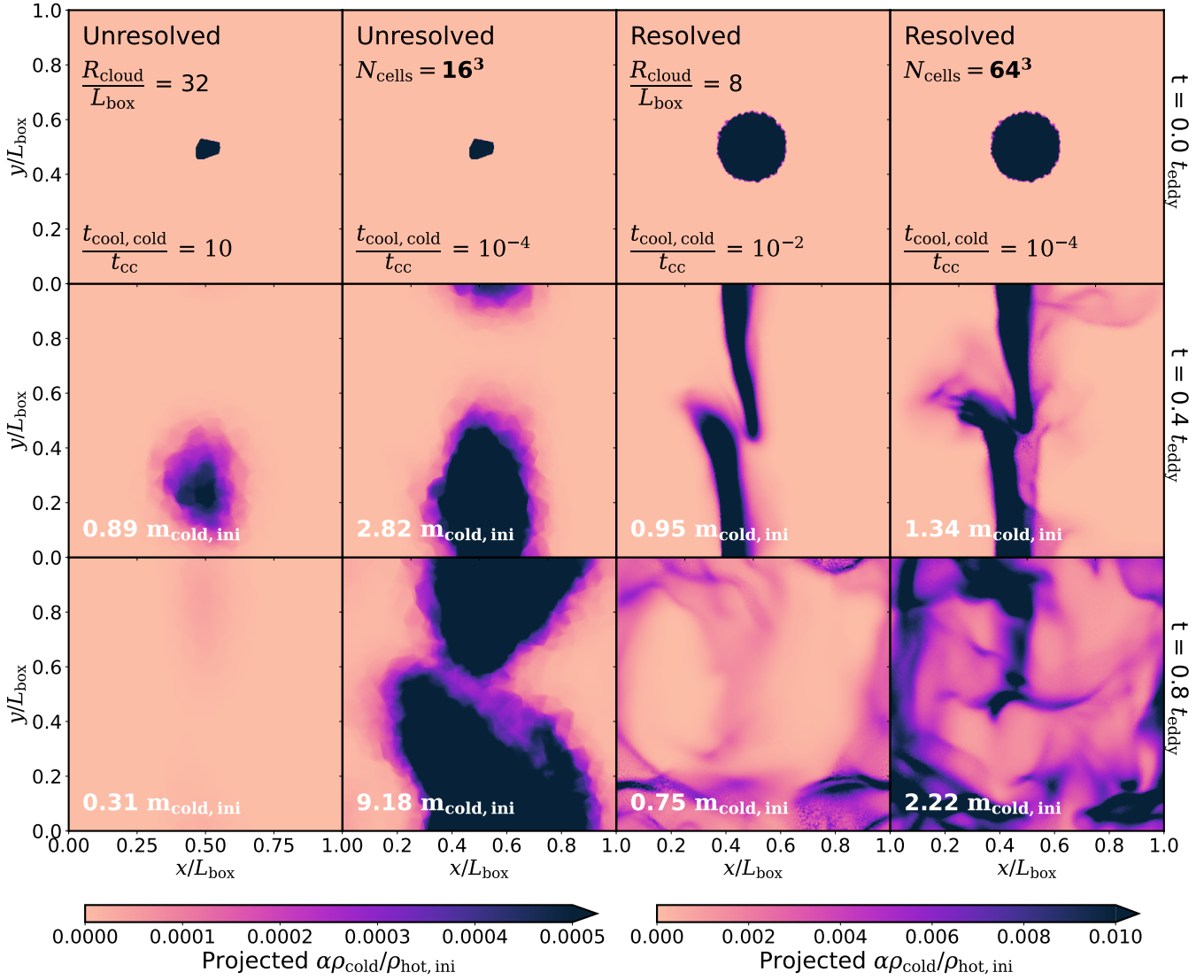


Figure 8. Projected $\alpha\rho_{\text{cold}}/\rho_{\text{hot, ini}}$, i.e. $\int_{\text{los}} \alpha(\rho_{\text{cold}}/\rho_{\text{hot, ini}}) dz/L_{\text{box}}$, plots at different times for MOGLI runs with $\mathcal{M} = 0.5$ different $t_{\text{cool,cold}}/t_{\text{cc}}$ values. Two columns on the left show the evolution of an unresolved ($L_{\text{box}}/R_{\text{cloud}} = 32$) initial cloud and two columns on the right show the evolution of a resolved initial ($L_{\text{box}}/R_{\text{cloud}} = 32$) cold cloud for destruction and survival regimes. We find that the clouds with short cooling timescales, i.e. $t_{\text{cool,cold}} = \{10, 10^{-2}\}t_{\text{cc}}$ survive and grow, while clouds with long cooling timescales, i.e. $t_{\text{cool,cold}} = 10^{-4}t_{\text{cc}}$ end up losing cold gas and get destroyed, as expected from the results of previous studies (Gronke et al. 2022).

in two sections. In this section, we test MOGLI with the Kolmogorov scaling-based turbulent velocity estimate. We use high-resolution Athena++ turbulent box simulations with resolved initial cold gas cloud as the benchmark to compare the multifluid simulations with the MOGLI subgrid model. For a model to be declared operational, we require the multifluid simulation to agree with the benchmark Athena++ simulations, even if the

- initial cold gas clump is resolved or unresolved, i.e., $R_{\text{cloud}}/dx > 1$ or < 1 , respectively.⁶,
- resolution of the simulation is varied (dx), regardless of the “resolvedness” of the cloud,

⁶ Note that throughout the text, we use R_{cloud} refers to the size of the initial cold gas cloud. l_{cold} in the previous section refers to the cold gas length scale inside a particular grid cell.

- turbulent velocity is changed (\mathcal{M}),
- random driving of the turbulence is different.

In the next sections, we test the different parts of the model across this parameter space. First, we only add the contributions from drag and turbulent mixing of cold gas and verify this reduced version of MOGLI with the benchmark Athena++ simulations in Sec. 4.1. In Sec. 4.2, we verify the full MOGLI model again with small-scale high-resolution Athena++ simulations and results.

4.1 Non-radiative Mixing

We start with testing a reduced version of the MOGLI model. This is to independently verify the different parts of the model. For the first set of tests, we only include the contributions from \dot{Q}_{drag} and \dot{Q}_{mix} , i.e. $\dot{Q}_{\text{non-rad}} = \dot{Q}_{\text{drag}} + \dot{Q}_{\text{mix}}$. This setup is analogous to

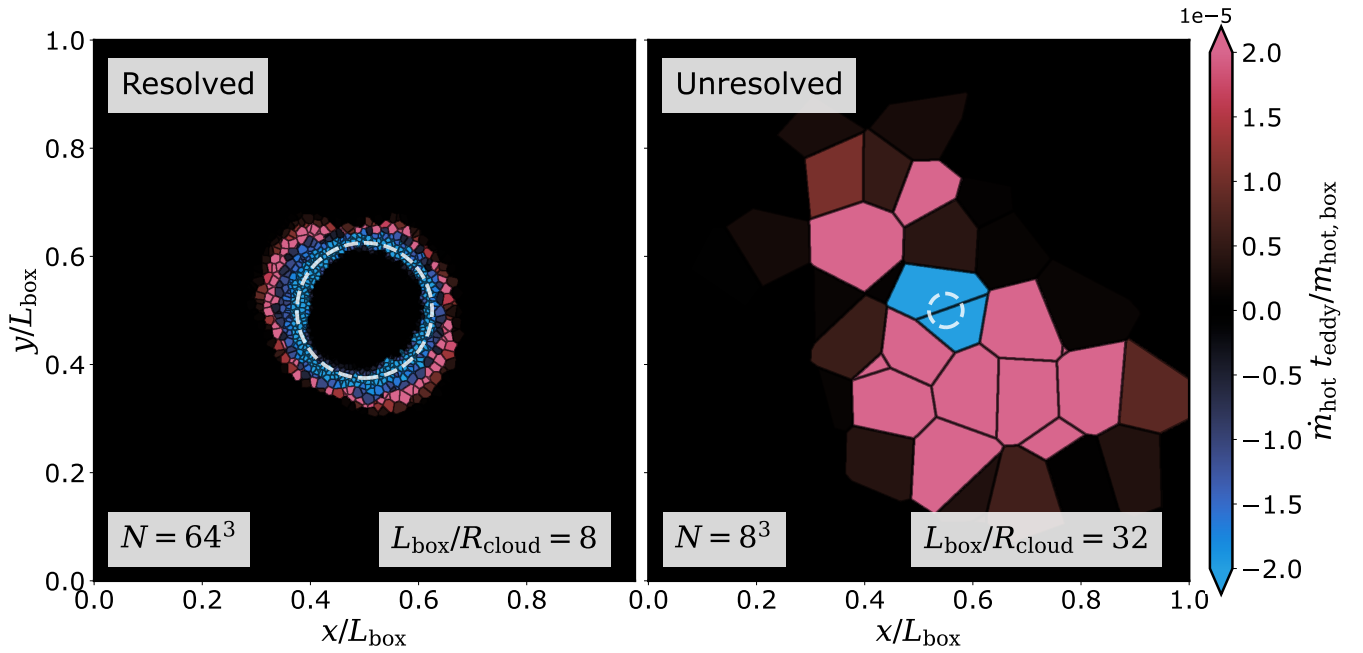


Figure 9. Early-time hot fluid mass flux (\dot{m}_{hot}) slices, normalised with ratio of total hot fluid mass and eddy-turnover time ($m_{\text{hot,box}}/t_{\text{eddy}}$), for MOGLI simulations with resolved and unresolved cold gas clouds, at $\mathcal{M} = 0.5$. The left panel shows an example of a resolved cold gas cloud with 64^3 cells and $L_{\text{box}}/R_{\text{cloud}} = 8$, where the cloud is bigger than the grid cells and grid cells inside the volume of the cloud have an $\alpha = 1 - \alpha_{\text{floor}}$. On the other hand, the right panel shows the slice for MOGLI simulation with an unresolved cold gas cloud, with 8^3 cells and $L_{\text{box}}/R_{\text{cloud}} = 32$. This shows how the model is able to distinguish between the interior and exterior of the resolved cloud and the mass exchange only occurs at the interface around the cloud. The dashed circles show the corresponding initial cold gas cloud size in the simulations.

the turbulent mixing of cold and hot gas in a non-radiative box, i.e. without radiative cooling.

We run the Athena++ turbulent box simulations and introduce a cold cloud after driving the turbulence, without radiative cooling. In the absence of cooling of the mixed gas, inevitably, the cold cloud loses mass at an approximately exponential rate. As shown in Fig. 6, we find the same behaviour in the MOGLI simulations with the subgrid model using $\dot{Q}_{\text{non-rad}}$. We vary the $L_{\text{box}}/R_{\text{cloud}}$ in the range [8, 64], resolution per direction in [8, 64], turbulent Mach number, \mathcal{M} in [0.2, 0.75] and random seed for turbulence driving.

In Athena++, we define cold gas mass as the total mass of gas cells with temperature below $8 \times 10^4 \text{K}$ and in MOGLI, the cold gas mass is the total mass of the cold fluid in the box. We calculate this for the snapshots separately and find the time taken for the total cold gas mass to reach half its initial value, i.e. t_{half} . Fig. 7 shows a scatter plot of the half mass time (t_{half}) normalised to the initial cloud-crushing timescale ($t_{\text{cc}} = \chi^{1/2} R_{\text{cloud}}/v_{\text{turb}}$)⁷, for different turbulent Mach numbers. As a benchmark, we use resolved Athena++ simulations with different resolutions (192^3 , 384^3 and 768^3 , represented by the colour of the point) and turbulence random seeds to capture the inherent stochasticity of cold gas destruction in a turbulent medium. Due to this inherent stochasticity, we show the mean and 2σ interval around the mean for the benchmark Athena++ and corresponding MOGLI simulations. For the MOGLI runs, the colour of the point in Fig. 7 shows how resolved or unresolved the initial cloud is via the ratio of the cloud radius and grid cell size (R/dx).

⁷ Throughout the text, t_{destroy} refers to the cold gas destruction timescale within the cell (cf. Eq. 12), while t_{cc} refers to the cloud destruction timescale of the initial cold gas cloud.

We find that the mean and scatter of the cold gas destruction from the subgrid model with the Kolmogorov turbulent velocity estimation agree well with the benchmark Athena++ and both cluster with a factor of ~ 2 near the analytical value of $\sim t_{\text{cc}}$. This verifies that the source function contribution for mixing, \dot{Q}_{mix} is working as expected and leads to a physically consistent behaviour.

4.2 Radiative mixing

Next, we include the remaining source function contribution for the growth of cold gas via mixing, \dot{Q}_{grow} . This gives us the full subgrid model for radiative mixing with $\dot{Q} = \dot{Q}_{\text{drag}} + \dot{Q}_{\text{mix}} + \dot{Q}_{\text{grow}}$. With the full subgrid model, the MOGLI simulations are analogous to resolved turbulent box simulations with radiative cooling, similar to simulations in Das & Gronke (2024); Gronke et al. (2022).

We run the MOGLI simulations with different turbulent Mach numbers (\mathcal{M}) in [0.2, 0.75], multiple resolutions per direction in [8, 64], two different random seeds for turbulent driving and different values of $t_{\text{cool,cold}}/t_{\text{cc}}$. We calculate the value of $t_{\text{cool,cold}}$ from the $t_{\text{cc}} = \chi^{1/2} R_{\text{cloud}}/v_{\text{turb}}$ and required value of their ratio. We use our Athena++ runs with different resolutions, turbulent Mach numbers random turbulence seeds, and cold cloud sizes (R_{cloud}) as the benchmark for comparison. This includes our simulations and the results from Gronke et al. (2022); Das & Gronke (2024).

4.2.1 Morphology

Fig. 8 shows the 2D maps of projected $\alpha\rho_{\text{cold}}$ ($\int_{\text{los}} \alpha\rho_{\text{cold}} dz/L_{\text{box}}$) plots at different times, for MOGLI runs with $\mathcal{M} = 0.5$ different $t_{\text{cool,cold}}/t_{\text{cc}}$ values. Two columns on the left show the evolution of

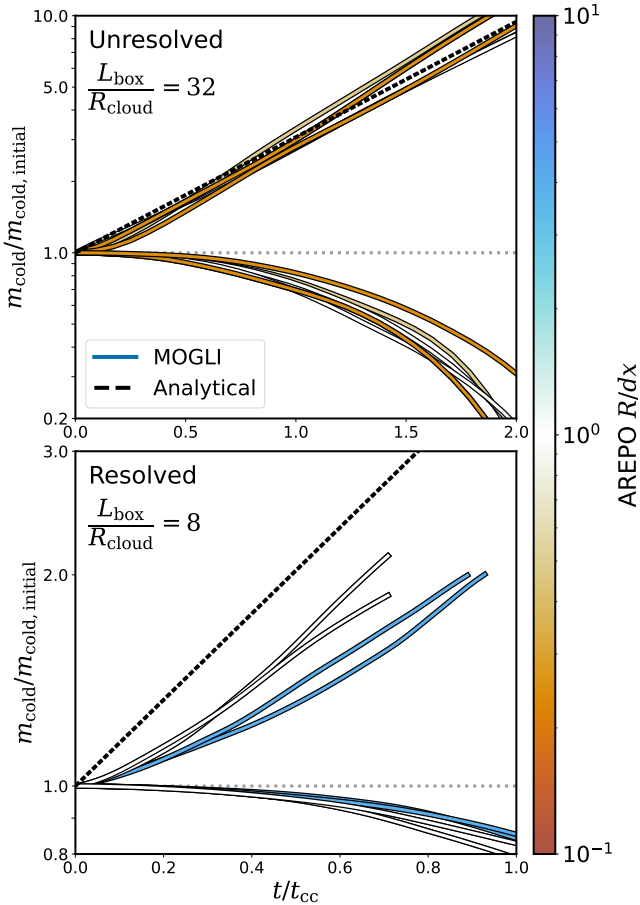


Figure 10. Cold gas evolution in MOGLI runs with time, normalised to the initial cloud-crushing time (t_{cc}), with $\mathcal{M}_{\text{turb}} = 0.5$. The two groups of curves correspond to $t_{\text{cool,cold}}/t_{cc} = \{10^{-4}, 10\}$. The solid lines show the cold gas evolution, as the total mass of the cold fluid, with the colour of the line denoting the initial R_{cloud}/dx . *Top panel* shows the evolution for simulations with unresolved initial cloud $L_{\text{box}}/R_{\text{cloud}} = 32$ and *bottom panel* shows the same for resolved initial cloud $L_{\text{box}}/R_{\text{cloud}} = 8$. The black dashed line shows the expected exponential growth of the simulations which grow, with the growth time (t_{grow}) calculated using Eq. (34). We find a good agreement between the analytically expected growth rates and MOGLI runs.

an unresolved ($L_{\text{box}}/R_{\text{cloud}} = 32$) initial cloud and two columns on the right show the evolution of a resolved initial ($L_{\text{box}}/R_{\text{cloud}} = 32$) cold cloud for destruction and survival regimes. We find that the clouds for runs with short $t_{\text{cool,cold}}$ show growth of cold gas, while the clouds in runs with longer $t_{\text{cool,cold}}$ get destroyed, as expected from the results of previous studies (Gronke et al. 2022).

Fig. 9 shows the early-time hot fluid mass flux (\dot{m}_{hot}) slices, normalised with ratio of total hot fluid mass and eddy-turnover time ($m_{\text{hot,box}}/t_{\text{eddy}}$), for radiative MOGLI simulations with resolved and unresolved cold gas clouds, at $\mathcal{M} = 0.5$. The left panel shows a case of a resolved cold gas cloud with 64^3 cells and $L_{\text{box}}/R_{\text{cloud}} = 8$, where the cloud is bigger than the grid cells and grid cells inside the volume of the cloud have an $\alpha = 1 - \alpha_{\text{floor}}$. It is clear that cells located within the cloud lose hot mass and gain cold mass ($\dot{m}_{\text{hot}} < 0$), while cold gas is being mixed into cells located just outside the cloud which thus gain hot mass and lose cold mass ($\dot{m}_{\text{hot}} > 0$).

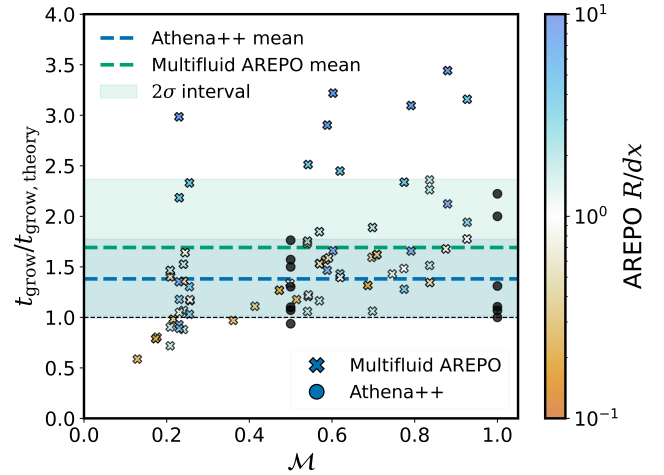


Figure 11. Scatter plot of the ratio of the t_{grow} from the simulations and the analytical $t_{\text{grow,theory}}$ (Eq. (34)), across different turbulent Mach number (\mathcal{M}). Crosses show the values from the MOGLI runs, with the colours denoting their "Resolvedness" (R/dx), while the black circles show the values from benchmark Athena++. The set of points for benchmark Athena++ include values calculated from simulations from Gronke et al. (2022); Das & Gronke (2024). We also show the means as dashed lines and 2σ intervals as shaded regions of the benchmark Athena++ and MOGLI runs. The comparison shows only a marginal difference between the benchmark Athena++ and MOGLI runs in the means with significant overlap between the scatter.

On the other hand, the right panel of Fig. 9 shows the slice from a MOGLI simulation with an unresolved cold gas cloud, 8^3 cells and $L_{\text{box}}/R_{\text{cloud}} = 32$. This shows how the model can distinguish between the interior and exterior of the resolved cloud and ensures that the mass exchange only occurs at the interface around the cloud. The dashed circles show the corresponding initial cold gas cloud size in the simulations.

4.2.2 Cold gas growth and survival

We use the same definition of cold gas as in Section 4.1, for both benchmark Athena++ runs and MOGLI runs to calculate the cold gas mass in different snapshots and obtain the evolution of cold gas mass with time. Fig. 10 shows the temporal evolution of the cold gas, normalised to the initial cold gas mass, in MOGLI runs with $\mathcal{M} = 0.5$. We include simulations with two different cold cloud sizes ($L_{\text{box}}/R_{\text{cloud}}$), two values for $t_{\text{cool,cold}}/t_{cc} = \{10^{-4}, 10\}$, two values for turbulence random seed and multiple resolutions. We only show the evolution till $m_{\text{cold,box}} < 0.9m_{\text{total,box}}$, as beyond that point the growth of the cold gas stagnates due to the deficiency of hot gas in the box and the theoretical predictions from previous studies do not apply anymore. The colour of the lines shows how "Resolved" ($R/dx > 1$) or "Unresolved" ($R/dx < 1$) the initial cold gas cloud is. We find that the MOGLI runs, regardless of the varied degrees of resolutions, also show growth of cold gas when $t_{\text{cool,cold}} \ll t_{cc}$ and destruction when $t_{\text{cool,cold}} \gg t_{cc}$, in agreement with the previous results using resolved single-fluid simulations (Gronke et al. 2022; Das & Gronke 2024).

In Fig. 10, we also show the corresponding analytical, cold gas growth curve as black dashed lines, and the MOGLI runs agree well with the predicted exponential growth curve. The analytical growth

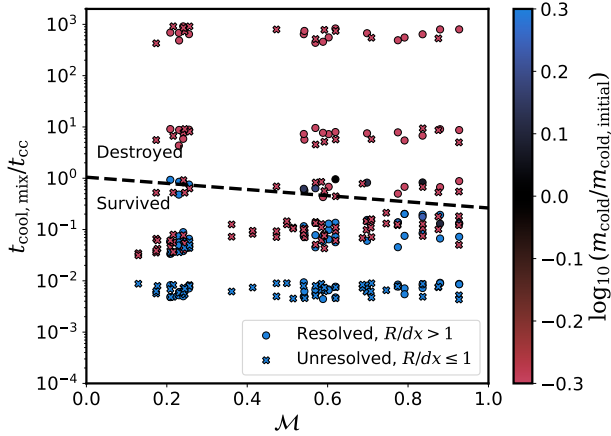


Figure 12. Scatter plot of survival or destruction of cold gas in the MOGLI runs, in a parameter space of $t_{\text{cool,mix}}/t_{\text{cc}}$ and turbulent Mach number, \mathcal{M} , where $t_{\text{cool,mix}}$ (c.f. Eq. (35)). The circles show the points from resolved ($R/dx > 1$) MOGLI simulations, while crosses denote the unresolved ($R/dx < 1$) simulations. The colour of the points denotes the ratio of total final cold fluid mass, averaged over the last 10 snapshots, normalised to the initial value. The black dashed line shows the survival criterion from Gronke et al. (2022), and we find that MOGLI can reproduce this survival criterion as an emergent behaviour. Note that the points are randomly shifted vertically by a factor of 1.5 for clarity.

timescale, $t_{\text{grow,theory}}$, is given by (Gronke et al. 2022)

$$\frac{t_{\text{grow,theory}}}{t_{\text{cc}}} = 0.5 \chi \left(\frac{t_{\text{cool,cold}}}{t_{\text{cc}}} \right)^{1/2} \left(\frac{L_{\text{box}}}{R_{\text{cloud}}} \right)^{1/6}. \quad (34)$$

Note that while this equation is of the same form as the implemented Eq. (17), on a per-cell basis, it is important to point out that whether our simulations recover the correct global growth rate is far from obvious.

Next, we quantitatively compare the cold gas growth rates between the benchmark Athena++ and the MOGLI runs. We calculate the cold gas mass doubling time and use it to calculate the t_{grow} . Fig. 11 shows the ratio of the t_{grow} from the simulations and the analytical $t_{\text{grow,theory}}$ from Eq. (34), across different turbulent Mach number (\mathcal{M}). Crosses denote the values from the MOGLI runs, with the colours denoting their "Resolvedness" (R/dx), while the black circles show the values from benchmark Athena++. The set of points for benchmark Athena++ include values of data from Gronke et al. (2022); Das & Gronke (2024). We also show the mean values as dashed lines and 2σ intervals as shaded regions, in blue for the benchmark Athena++ and in green for MOGLI runs. The comparison shows only a marginal difference in the means with significant overlap between the scatter of values from benchmark Athena++ and MOGLI runs. This verifies that the MOGLI subgrid model accurately captures the growth of cold gas to a reasonable extent.

Apart from growth rates, a working subgrid model should consistently agree with the survival criterion of cold gas clouds obtained in previous studies using resolved single-fluid simulations (Gronke et al. 2022). In Fig. 12, we reproduce the survival plot from Gronke et al. (2022) with MOGLI runs. It shows the survival or destruction of cold gas in the MOGLI runs, in a parameter space of $t_{\text{cool,mix}}/t_{\text{cc}}$ and turbulent Mach number (\mathcal{M}), where $t_{\text{cool,mix}}$ refers to the cooling

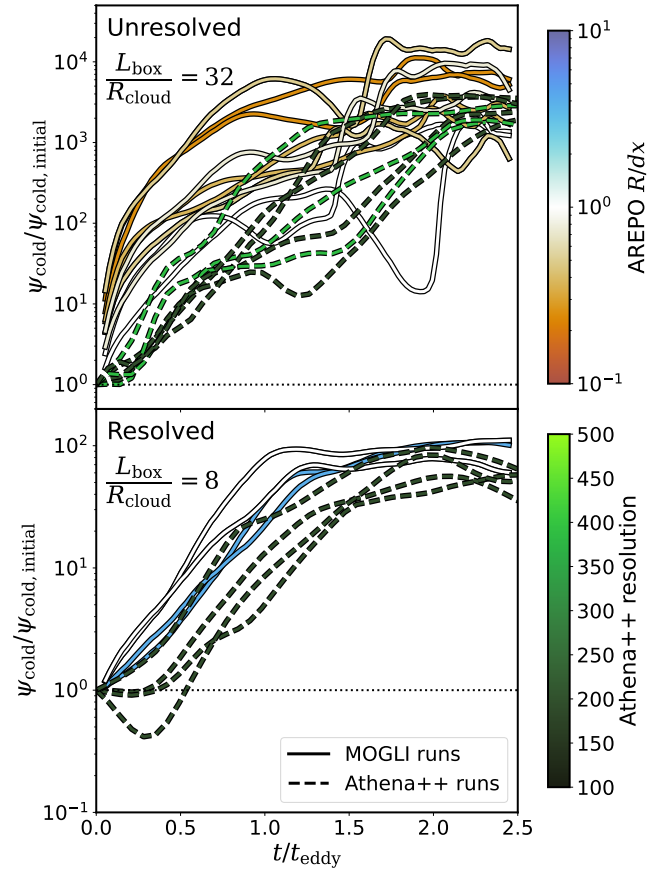


Figure 13. Evolution of the cold gas dispersion, normalised to its initial value, in the benchmark Athena++, as dashed lines, and MOGLI runs, as solid lines, with time normalised with turbulent eddy turnover time. The colour of dashed lines shows the resolution of the Athena++ simulations, while the colour of the solid lines shows the "resolvedness" of the initial cold cloud in the MOGLI runs, i.e. R/dx . Left panel shows the evolution of MOGLI runs with resolved initial clouds at $L_{\text{box}}/R_{\text{cloud}} = 8$, and the corresponding Athena++ runs. Right panel shows the same but for MOGLI runs with unresolved initial cloud at $L_{\text{box}}/R_{\text{cloud}} = 32$, and the Athena++ runs.

time of the intermediate mixed gas,

$$t_{\text{cool,mix}} = t_{\text{cool}}(T_{\text{mix}}, \rho_{\text{mix}}) \quad (35)$$

where the $T_{\text{mix}} = \sqrt{T_{\text{cold}}T_{\text{hot}}}$ and $\rho_{\text{mix}} = \sqrt{\rho_{\text{cold}}\rho_{\text{hot}}}$ are the temperature and density of the intermediate mixed gas (Begelman & Fabian 1990).

As the MOGLI runs only use the cold gas cooling time ($t_{\text{cool,cold}}$), unlike our Athena++ runs which use a full cooling function, we assume the CIE cooling curve from Wiersma et al. (2009) (as used in the benchmark Athena++ runs) to evaluate $t_{\text{cool,mix}} = \chi t_{\text{cool,cold}} \Lambda(T_{\text{mix}})/\Lambda(T_{\text{cold}})$. For our choice of T_{cold} , χ this results in $t_{\text{cool,mix}} \approx 64 t_{\text{cool,cold}}$

The circles in Fig. 12 denote runs with "resolved" ($R/dx > 1$) initial cold clouds and crosses represent the "unresolved" ($R/dx \leq 1$) initial cold clouds and the colour of the points show the final cold gas mass, averaged over the last 10 snapshots and normalised with the

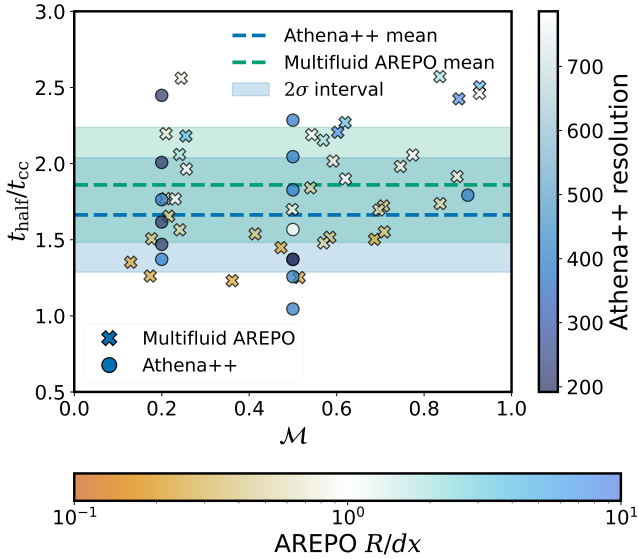


Figure 14. Same as Fig. 7 but with the gradient-based local turbulence estimation. Scatter plot of the half mass time (t_{half}) normalised to the initial cloud-crushing timescale ($t_{\text{cc}} = \chi R_{\text{cloud}}/v_{\text{turb}}$), for different turbulent Mach numbers. Athena++ simulations with different resolutions (192^3 , 384^3 , and 768^3 , represented by the colour of the point) and turbulence random seeds to capture the inherent stochasticity of cold gas destruction in a turbulent medium.

initial cold gas mass. We show the survival criterion found in Gronke et al. (2022) and confirmed in Das & Gronke (2024) as a dashed black line along with annotation for the survival and destruction regimes. As there are a large number of points with very similar parameters, we randomly displace the points vertically by a factor of 1.5, for clarity. We find that the MOGLI runs agree well with the survival criteria. We also see some stochasticity in simulations that lie close to the criterion. This is an expected behaviour seen in resolved single-fluid simulations due to the inherent randomness of turbulence. This verifies the ability of the subgrid model to accurately reproduce the survival and destruction of cold gas as an emergent behaviour.

4.2.3 Cold gas dispersion

As the simulation evolves, the cold gas is expected to get progressively more dispersed with time and can be an important mechanism for the transport of cold gas in large-scale simulations. We test for differences in the dispersion of cold gas in the benchmark Athena++ and MOGLI simulations. We define a quantity, ψ , as a proxy for the dispersion of cold gas,

$$\psi_{\text{cold}} = \prod_{i=[1,2,3]} \left[\frac{\sum_{\text{cold}} m_{\text{cold}} \delta x_{i,\text{com}}}{\sum_{\text{cold}} m_{\text{cold}}} \right] \quad (36)$$

where, $\delta x_{i,\text{com}} = |x_{i,\text{cell}} - x_{i,\text{com,cold}}|$ is the distance, along i^{th} axis, between the cold gas/fluid centre-of-mass and cell centre, in a periodic box. We run benchmark Athena++ and the corresponding MOGLI runs with initial $R_{\text{cloud}}/l_{\text{shatter}} = 310$, varying resolution and different turbulent random seed. We repeat this calculation on the snapshots from Athena++ and MOGLI runs to obtain the temporal evolution of the cold gas dispersion (ψ_{cold}). Fig. 13 shows the temporal evolution of the ψ_{cold} , normalised to its initial value, in the benchmark Athena++ as dashed lines, and MOGLI runs as

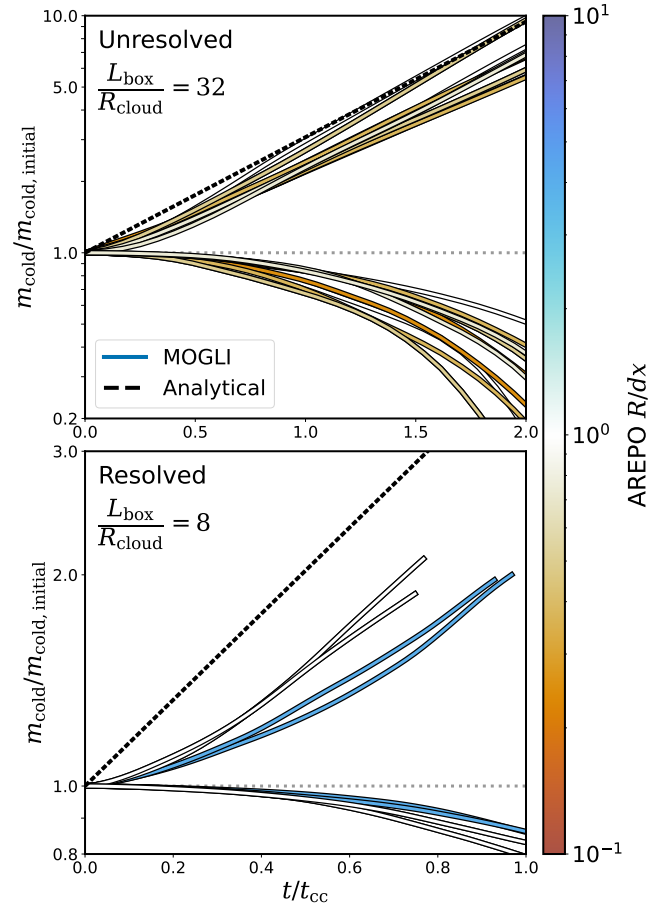


Figure 15. Same as Fig. 10 but with the gradient-based local turbulence estimation. Cold gas evolution in MOGLI runs with time, normalised to the initial cloud-crushing time (t_{cc}), with $\mathcal{M}_{\text{turb}} = 0.5$. The two groups of curves correspond to two different values of $t_{\text{cool,cold}}/t_{\text{cc}} = \{10^{-4}, 10\}$. The solid lines show the cold gas evolution, as the total mass of the cold fluid, with the colour of the line denoting the initial R_{cloud}/dx . Top panel shows the evolution for simulations with unresolved initial cloud $L_{\text{box}}/R_{\text{cloud}} = 32$ and bottom panel shows the same for resolved initial cloud $L_{\text{box}}/R_{\text{cloud}} = 8$. The black dashed line shows the expected exponential growth of the simulations which grow, with the growth time (t_{grow}) calculated using Eq. (34). We find a good agreement between the analytically expected growth rates and MOGLI runs.

solid lines. The colour of dashed lines shows the resolution of the Athena++ simulations, while the colour of the solid lines shows the “resolvedness” of the initial cold cloud in the MOGLI runs, i.e. initial R/dx . The top panel shows the evolution of MOGLI runs with unresolved initial clouds at $L_{\text{box}}/R_{\text{cloud}} = 32$, and the corresponding Athena++ runs. The bottom panel shows the same but for MOGLI runs with unresolved initial cloud at $L_{\text{box}}/R_{\text{cloud}} = 8$, and the Athena++ runs.

In general, in both “resolved” and “unresolved” cloud cases, while the cold gas dispersion is higher in MOGLI runs, the growth of dispersion follows qualitatively similar evolution with similar timescales. The higher dispersion is likely due to the poorer resolution for the highly unresolved, i.e. low R/dx , which leads to higher numerical diffusion in volume fraction. This can be improved in future with a higher-order solver in the multifluid code, but the differences fall within an acceptable range for the current study.

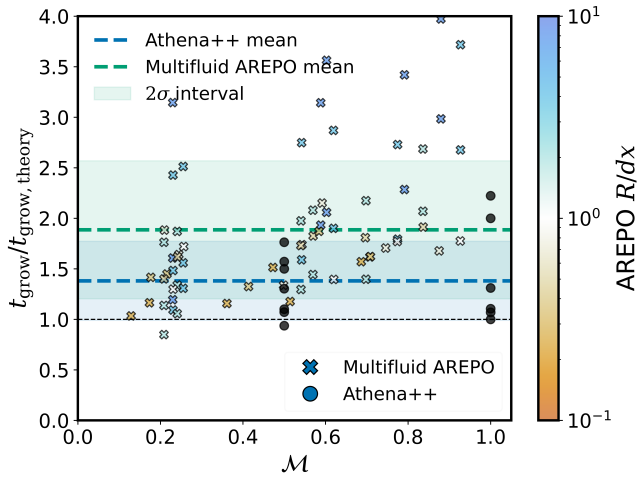


Figure 16. Same as Fig. 11 but with the gradient-based turbulence estimation. Scatter plot of the ratio of the t_{grow} from the simulations and the analytical $t_{\text{grow,theory}}$ (Eq. 34), across different turbulent Mach number (\mathcal{M}). Crosses show the values from the MOGLI runs, with the colours denoting their "Resolvedness" (R/dx), while the black circles show the values from benchmark Athena++. The set of points for benchmark Athena++ include values calculated from simulations from Gronke et al. (2022); Das & Gronke (2024). We also show the means as dashed lines and 2σ intervals as shaded regions of the benchmark Athena++ and MOGLI runs. The comparison shows only a marginal difference between the benchmark Athena++ and MOGLI runs in the means with significant overlap between the scatter.

With the above tests, we verify that the MOGLI model, with the Kolmogorov turbulence estimation, can capture all the different facets of cold gas behaviour, i.e. the survival, destruction rates, growth rates and cold gas dispersion in a turbulent medium, in an emergent way. In the next section, we repeat the verification tests from this section for MOGLI model with our new gradient-based local turbulence estimation method (grad).

5 VERIFICATION: WITH VELOCITY GRADIENT-BASED TURBULENCE ESTIMATION

As the Kolmogorov estimation method (ko1) assumes isotropic and steady-state turbulence over the simulation domain, it cannot be applied in setups with evolving or strongly varying turbulence. For more general scenarios with temporal and/or spatial variation in turbulence, we need a method to estimate the local turbulent velocity from the local fluid properties. We implement the grad method for local turbulence estimation based on velocity gradients to get around this limitation of the ko1 method. As described in Sec. 3.6.2, we use the local velocity gradient calculated using neighbouring cells in AREPO (Pakmor et al. 2016) to estimate the velocity dispersion in the neighbourhood. Once we know the turbulent velocity in this neighbourhood, we scale it to the cold gas scales by assuming a fully developed Kolmogorov turbulence below those grid scales.

We repeat our verification tests from Section 4 to confirm the accuracy of MOGLI with the gradient-based turbulent velocity estimation. We start with checking the non-radiative turbulent mixing rates. Fig. 14, analogous to Fig. 7, shows the cold gas half time for non-radiative MOGLI runs ($\dot{Q} = \dot{Q}_{\text{drag}} + \dot{Q}_{\text{mix}}$) with the grad method. For the grad method, we find a slightly higher separation between the mean of the benchmark Athena++ and MOGLI runs,

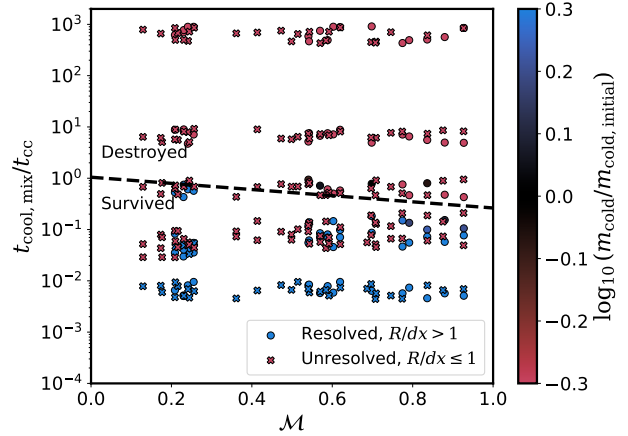


Figure 17. Same as Fig. 12 but with the gradient-based turbulence estimation. Scatter plot of survival or destruction of cold gas in the MOGLI runs, in a parameter space of $t_{\text{cool,mix}}/t_{\text{cc}}$ and turbulent Mach number, \mathcal{M} , where $t_{\text{cool,mix}}$ (c.f. Eq. (35)). The circles show the points from resolved ($R/dx > 1$) MOGLI simulations, while crosses denote the unresolved ($R/dx < 1$) simulations. The colour of the points denotes the ratio of total final cold fluid mass, averaged over the last 10 snapshots, normalised to the initial value. The black dashed line shows the survival criterion from Gronke et al. (2022), and we find that MOGLI can reproduce this survival criterion as an emergent behaviour. Note that the points are randomly shifted vertically by a factor of 1.5 for clarity.

and a wider scatter in both cases when compared to the ko1 method of estimation. The differences are minimal and within acceptable limits. So, we can conclude that the grad method works well for non-radiative mixing.

For the full model, i.e., including radiative mixing, first, we check the evolution of cold gas mass evolution in Fig. 15, analogous to Fig. 10. It shows the same behaviour where, regardless of the resolution, the clouds with faster cooling time, i.e. $t_{\text{cool,cold}}/t_{\text{cc}} \ll 1$, grow at expected rates while the clouds with slow cooling, i.e. $t_{\text{cool,cold}}/t_{\text{cc}} \gg 1$, get destroyed. Subsequently, we repeat the quantitative verification of the growth rates in Fig. 16, similar to the comparison made in Fig. 11. We find marginally higher differences in the mean value of $t_{\text{grow}}/t_{\text{grow,theory}}$ (cf. Sec. 4.2.2) of the benchmark Athena++ runs and MOGLI runs, in comparison to the differences with ko1 method, while the standard deviation is similar.

Next, we verify the emergent survival criterion from MOGLI with the grad estimation. In Fig. 17, we show the survival and destruction of the cold cloud, analogous to Fig. 12. We find that the MOGLI runs still agree well with the survival criterion from Gronke et al. (2022), albeit slightly worse than the ko1 method.

Finally, we check for any differences in the dispersion of cold fluid using the local turbulent estimator. Fig. 18 shows the evolution of cold gas dispersion ψ_{cold} (cf. Eq. 36 in Sec. 4.2.3), analogous to Fig. 13 for ko1 method. We find that the cold gas dispersion follows an almost identical evolution with grad method, in Fig. 18 as with grad in Fig. 13.

With the series of tests above, we can conclude that MOGLI model with the velocity gradient-based local turbulence estimation (grad) method also accurately captures the subgrid behaviour of cold gas with a good agreement with the benchmark Athena++ and analogous MOGLI runs with the ko1 simulations. Since the average turbulence estimates are consistent and the agreement between MOGLI and the

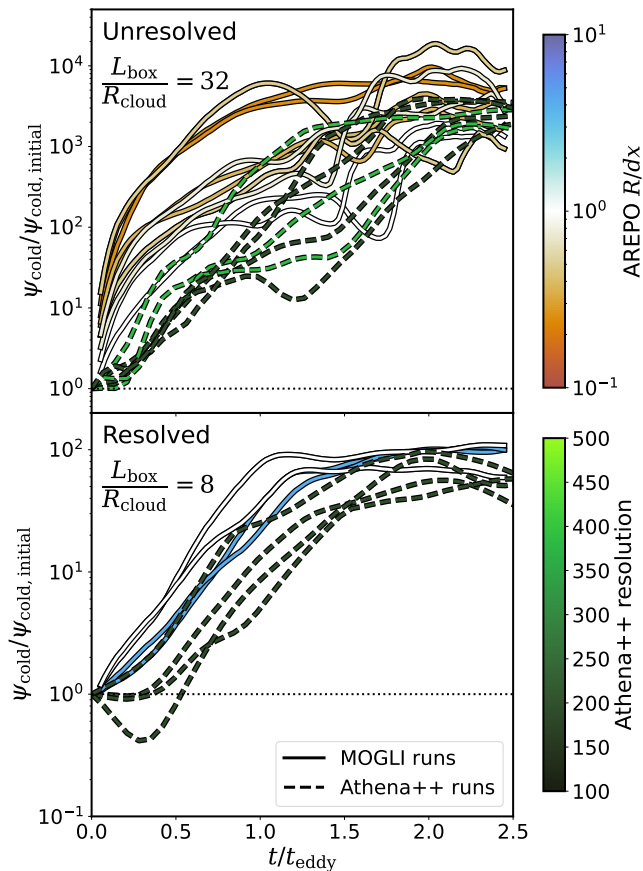


Figure 18. Same as Fig. 13 but with gradient-based turbulence estimation. Evolution of the cold gas dispersion, normalised to its initial value, in the benchmark Athena++, as dashed lines, and MOGLI runs, as solid lines, with time normalised with turbulent eddy turnover time. The colour of dashed lines shows the resolution of the Athena++ simulations, while the colour of the solid lines shows the “resolvedness” of the initial cold cloud in the MOGLI runs, i.e. R/dx . *Top panel* shows the same but for MOGLI runs with unresolved initial cloud at $L_{\text{box}}/R_{\text{cloud}} = 32$, and the Athena++ runs. *Bottom panel* shows the evolution of MOGLI runs with resolved initial clouds at $L_{\text{box}}/R_{\text{cloud}} = 8$, and the corresponding Athena++ runs.

resolved Athena++ runs was demonstrated in the previous section, this outcome is unsurprising. However, this assumption does not hold for simulations focused on local measures (e.g., local dispersion) or where gas flows vary significantly, making a ‘global’ concept of turbulence inapplicable. In summary, we find the grad method to be more suitable for most astrophysical applications and thus adopt it as the default in MOGLI. Nonetheless, the initial comparison with the simpler ko1 method provides a valuable opportunity to isolate and understand the underlying physical mechanisms.

6 DISCUSSION

6.1 Model showcase

After the testing and verification of the MOGLI model in Sec. 4 & 5, we can use it to simulate a setup to show the strengths of such a model. We simulate a turbulent box with 64^3 cells and $\mathcal{M} = 0.5$, and introduce 100 unresolved clouds with a radius of $L_{\text{box}}/256$, where L_{box} is the box size. To run an analogous setup in a single-fluid simulation code without a subgrid model, we need to resolve the individual clouds with around 10 cells across their radius, hence requiring a single-fluid simulation with $\sim 3000^3$ cells. Such single-fluid simulations require a considerable computational cost, while our analogous MOGLI multifluid simulation can capture the relevant cold gas evolution with just a 64^3 cells simulation with negligible computational cost. Fig. 19 shows the evolution projected $\alpha\rho_{\text{cold}}/\rho_{\text{hot,ini}}$ for the showcase simulation using our MOGLI model with the grad local turbulence estimation method.

This shows the potentially massive savings in computational times with the MOGLI model, over a brute force method of resolving the cold gas structures in a single-fluid code without a subgrid model allowing for configurations infeasible with traditional single-fluid simulations. We plan to study several such scenarios in future work.

6.2 The need for a multiphase subgrid model

With the ISM, CGM, and ICM, multiphase media are ubiquitous in and around galaxies and, thus, crucial to our understanding of galaxy formation and growth. Not only is the new fuel for star-formation channelled through the multiphase galactic halos (see reviews by Donahue & Voit 2022; Faucher-Giguère & Oh 2023) but gas is also expelled from galaxies through multiphase galactic winds (Veilleux et al. 2020; Heckman & Thompson 2017). Even the gas within the galaxy is highly multiphase with a much wider range of temperatures, from $\sim 10^2\text{K}$ gas in molecular gas to $> 10^7\text{K}$ gas in supernova ejecta. Thus, correctly modelling multiphase gas dynamics is the foundation of accurately modelling gas transport, its conversion into stars and their subsequent impact on the galaxy when they end in supernovae and lead to feedback. Hence, understanding multiphase gas is a cornerstone of understanding the wider baryon cycle.

While great strides are being made to model the interstellar medium including its multiphase nature correctly in dedicated, small domain simulations (Walch et al. 2015; Kim & Ostriker 2017), this is much more problematic in a larger scale, cosmological simulations. Nevertheless, modern large-scale cosmological simulations using ‘zoom in’ and adaptive techniques, based on targeting a mass resolution, manage to reach a parsec-scale resolution in certain dense regions within the ISM while at the same time capturing the effects of the larger environment.

However, the same techniques cannot be applied to the halo of galaxies spanning $\sim 100\text{kpc}$ in radius (for a Milky Way-sized galaxy at $z \sim 0$; Tumlinson et al. 2017). In these large volumes, recent observations constrain the upper limit to the size of this cold gas to be $\lesssim 10\text{pc}$ (Lan & Fukugita 2017; Crighton et al. 2015; Schaye et al. 2007; Rauch et al. 1999). This implies that simulation of a single halo would require at least $(100,000)^3$ resolution elements – a task infeasible even for the next generation of supercomputers. For example, modern cosmological simulations require tens of millions of CPU hours to simulate $\sim 10^9$ particles/cells (e.g., Thesan, Kannan et al. 2022). Extrapolating this figure to $(100,000)^3$ cells, we would need $\sim 10^7$ million core hours. Thus, even an optimally parallelised run on one million cores (approximately the number of CPU cores on

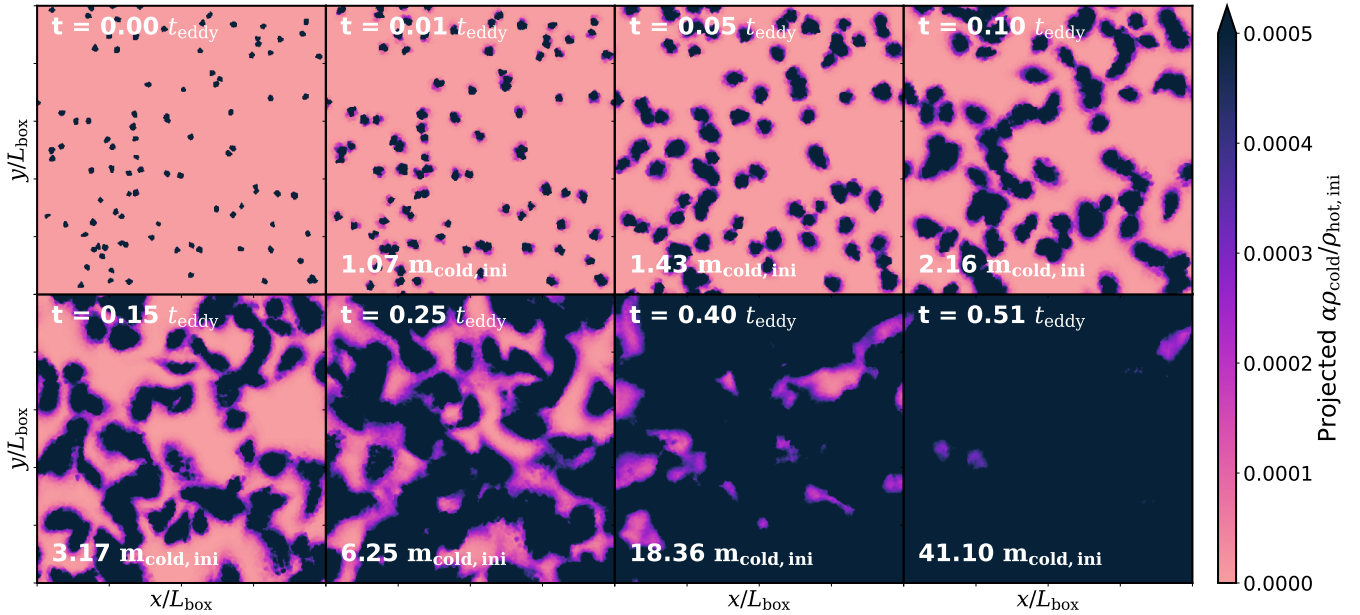


Figure 19. Evolution of projected $\alpha\rho_{\text{cold}}/\rho_{\text{hot,ini}}$ for a turbulent box with MOGLI, grad method, 64^3 cells, 100 unresolved clouds with a radius $L_{\text{box}}/256$, where L_{box} is the box size, and $t_{\text{cool}}/t_{\text{cc}} = 5 \times 10^{-4}$. The unresolved clouds grow and subsequently fill the box due to its finite size. We will need a box with $\sim 3000^3$ cells to run an analogous simulation in a single-fluid code without a subgrid model.

the exascale supercomputer El Capitan) such a run would take 10^7 hours, i.e. ~ 1000 years. Of course, this is a simplified approximation; however, it still illustrates the point that even next-generation exascale machines will not be able to resolve the CGM structure observed to date.

The inability of modern cosmological simulations to achieve the resolution needed to model the (observed) cold gas structures found in the halos directly comes from the fact they are non-converged in even the most basic cold gas properties such as the amount of $\sim 10^4$ K gas found (see extensive discussion of this in the literature, e.g., Faucher-Giguère & Oh 2023; van de Voort et al. 2021; Hummels et al. 2024; Ramesh & Nelson 2024; Peebles et al. 2019). This implies that when comparing such simulations to CGM observables, it is impossible to know whether a (mis)match is due to the physics implemented in this simulation (e.g., the feedback mechanisms, and star formation models) or if this is a transient agreement that would vanish with a higher resolution.

In addition, while the simulation projects mentioned above can significantly increase the number of resolution elements in the CGM, it is important to note that all these projects start with cosmological zoom simulations of individual halos in which memory usage is not as much of an issue. However, to study cold gas microphysics across the galaxy population, this technique would have to be applied to a large number of halos, posing significant additional requirements on the available memory. Since modern uniform mass resolution galaxy formation simulations are limited not solely by compute resources but also by memory, such an undertaking would only allow very limited increases in the number of resolution elements per halo, with no prospects to resolve the required spatial scales any time soon.

This limitation due to a highly multiscale problem is not new to astrophysics. For about two decades now, we have known that supernovae feedback – taking place on initially minuscule scales – is crucial to shaping galaxy morphology (e.g. Naab & Ostriker 2017). The way these indispensable ‘feedback’ processes are modelled in

astrophysical simulations is through a ‘subgrid model’, that is, by including their effects on larger scales through (empirical) source and sink terms.

Our model MOGLI is exactly such a subgrid model but for a two-phase multifluid medium. While it is not the first model of this kind (cf. § 6.3 for a comparison to previous work), it includes (i) a solid Eulerian-Eulerian numerical framework common in engineering (Weinberger & Hernquist 2023) implemented in the popular code AREPO (Weinberger et al. 2020; Springel 2010), and (ii) coupling terms between the phases based on and verified with small-scale simulations and combustion inspired theory (Tan et al. 2021; Gronke et al. 2022).

This solid foundation implies that the number of free parameters in our model is at a bare minimum, i.e. it includes only two free parameters. Only in Eq. (15), the $\dot{m}_{\text{cold}\rightarrow\text{hot}}$ includes a fudge parameter for the α_{mass} threshold, and in Eq. (29), $v_{\text{turb,grad,MOGLI}}$ includes ξ_{MOGLI} (which is within a factor of ~ 2 of the theoretically expected value). Such a low number of free parameters is important, in general, for a subgrid model to preserve the predictive power of the simulations – but especially for a multiphase subgrid model such as MOGLI, as all cells are affected by it. Thus, allowing for more degrees of freedom by, for example, altering directly the amount of cold gas found in the halo would diminish the predictive power rapidly.

Naturally more work is required (cf. § 6.4) but this work is a strive in the right direction to ultimately model the multiphase gas in and around galaxies in a converged manner.

6.3 Previous work

As multiphase media are common in terrestrial applications, numerical tools to model them are extensively developed and widely used in various engineering disciplines, such as chemical, mechanical, and civil engineering. For example, in chemical engineering, they are critical for simulating processes like distillation, fluidized bed reac-

tors, and mixing in multiphase reactors. In mechanical engineering, they enable the design and optimization of cooling systems involving liquid-vapor interactions, such as in heat exchangers and condensers. In civil engineering, they play a key role in understanding and managing subsurface flows, including groundwater contamination, oil recovery, and sediment transport in rivers (Prosperetti & Tryggvason 2007).

In astrophysics, however, dedicated methods to model multiphase flows are less used – with some notable exceptions. Semelin & Combes (2002), for instance, already included a ‘warm’ ($> 10^4$ K) and a ‘cold’, pressureless phase as two separate fluids in their SPH scheme (alongside stars and dark matter) with the colder one being modelled via a ‘sticky particle scheme’ (Levinson & Roberts 1981), thus, allowing the particles to inelastically collide with each other. They include the possibility for ‘warm’ particles to cool down and turn into ‘cold’ ones, and vice-versa to evaporate ‘cold’ particles due to supernovae feedback. Using this scheme, Semelin & Combes (2002) successfully perform a simulation of an isolated disk galaxy and study its evolution. While their source/sink terms are relatively large-scale and simplified, their approach represents a pioneering step toward incorporating multiphase processes in galaxy modelling (also see Berczik et al. 2003 for a similar implementation or Harfst et al. 2004 for an extension to three phases).

A similar approach is followed by Scannapieco et al. (2006), who instead of using two different particle types in their SPH scheme, ‘decouple’ particles with low entropy (essentially corresponding to a cold phase), thus, allowing neighbouring particles with different thermal properties. This implementation is meant to address the ‘overcooling problem’ where the energy of a supernova ejected in the dense medium is instantly lost (e.g. Kim & Ostriker 2015; Smith et al. 2018). While the multiphase implementation of Scannapieco et al. (2006) is not specifically targeting galactic winds, their supernovae feedback implementation results in a separation of nearby particles into ‘hot’ and ‘cold’ ones, and, thus leads to an efficient wind launching. Their algorithm can thus be seen to be more in line with the more recent developments of SN ejected winds where particles are also decoupled (Springel & Hernquist 2003; Okamoto et al. 2005; Oppenheimer & Davé 2006).

More recently, the multiphase nature of galactic winds has led to the development of several Eulerian-Lagrangian subgrid models where the cold phase is represented by particles within a hot gas cell (Huang et al. 2020; Smith et al. 2024). In these models, physically motivated source and sink terms between the phases akin to the ones used in this study have been implemented. However, as the particles representing the cold phase have zero extents, reproducing the dispersion of the cold medium (cf. § 4.2.3) would require particle splitting/merging which is currently not implemented in these models.

Our work can be seen as a continuation of these efforts. While the previous astrophysical work mentioned above has focused on a colder phase represented via a particle, we have created a two-phase (a $\sim 10^4$ K and a ‘hot’ $\gtrsim 10^6$ K phase) Eulerian-Eulerian subgrid model using the multifluid implementation of Weinberger & Hernquist (2023) and coupling terms inspired by combustion theory which was validated previously using a range of small-scale numerical simulations (Ji et al. 2019; Tan et al. 2021; Gronke et al. 2022; Tan et al. 2023). This implementation has the advantage that it can especially capture multiphase, turbulent media – which are ubiquitously found in astrophysics, such as in the CGM, ICM and galactic winds – as well as the cold gas disperses naturally.

In this regard, our approach is similar to the two-fluid model implemented in ENZO by Butsky et al. (2024) during the work on

this model. Note, however, that our cold fluid is represented as a compressible second fluid while their cold phase is assumed to be pressureless. While both should yield the same result in the case of vanishing volume filling fractions and temperature of the cold phase, a pressureless fluid can only represent unresolved cold clouds. The transition to marginally resolved or even fully resolved clouds where the pressure of the cold fluid displaces the hot fluid, i.e. the main focus of this work, cannot be modelled in the pressureless approach. This also results in differences in source terms: their coupling terms between the phases are inspired by the classical ‘cloud crushing’ problem, i.e., the interaction of a laminar hot wind and a cold cloud (e.g., Klein et al. 1994) with the individual cold gas cloudlets radii being $r_{\text{cl}} \approx \min(c_s t_{\text{cool}})$ inspired by the ‘shattering’ scenario (McCourt et al. 2018). In contrast, the presented work allows full flexibility in the respective volume filling fractions and allows, specifically, also the case where the typical length and timescales of unresolved and resolved processes are comparable. Thus, we needed to generalise the source terms to account for the finite availability of hot gas, of ‘shielding’ of inner layers of resolved cold clouds and geometric considerations of the change in surface area when a substantial fraction of a cell is filled with cold gas and generally cannot assume an instantaneous equilibration of the cold gas into a universal cloud radius or cloud mass function.

6.4 Limitations and future directions

Although our model MOGLI takes a step in the direction of capturing the rich physics of small-scale cold gas structures, many aspects of the multiphase gas are still open questions and remain to be investigated in both small-scale simulations and subgrid modelling. Some of such aspects are:

- *Magnetic fields*: Although magnetic fields can suppress mixing via hydrodynamical instabilities like Kelvin-Helmholtz instabilities (Chandrasekhar 1961; Ji et al. 2019), as shown in Das & Gronke (2024), the mixing properties depend only on the turbulent velocities. Hence, MOGLI model should remain unchanged with or without magnetic fields.
- *Thermal conduction*: In the turbulent mixing of cold gas, the eventual mixing of cold gas is via thermal conduction at molecular diffusion scales. Such small scales are not resolved in our simulations, but as shown in Tan et al. (2021), the turbulent mixing is rate-limited at the scales of the largest eddy, and is converged with the largest eddy scales are well resolved. Although, in our simulations, the thermal conduction is numerical, due to the rate-limiting nature of the largest scale, we expect the multiphase gas behaviour to be unchanged.
- *Viscosity*: Similar to thermal conduction, viscosity operates at very small scales and can change the small-scale turbulent properties. Even though we have numerical viscosity in our simulations, due to the same rate-limiting nature of largest eddies in turbulent mixing, with grid cells larger than the viscous scales, the multiphase gas properties are expected to be unaffected⁸.

Apart from the limitations mentioned above, there are many directions the MOGLI can be expanded in future studies. Currently, MOGLI does not account for in-situ formation of cold gas from hot

⁸ Note, however, that viscosity can change the microturbulent properties of the ‘laminar’ cooling front on small scales, and thus, potentially affect the form of our coupling terms (cf. Tan et al. 2021). This will need to be checked explicitly with small-scale simulations in the future (Marin-Gilabert et al., in prep.).

gas via processes like thermal instability (Field & Field 1965; McCourt et al. 2018; Sharma et al. 2010). This will enable the creation of the initial seed cold gas which can later grow further via turbulent mixing included in the MOGLI model.

Another avenue for refining the model is the inclusion of other phases. It is clear from observations that colder ($< 8000\text{K}$) gas exists (McKee & Ostriker 1977; Cox 2005), which points to the existence of a three-phase gas, with much more rich physics and complex interactions among the phases (Farber & Gronke 2021; Chen & Oh 2024). Three-phase turbulent gas is still a relatively unexplored system and detailed investigations with small-scale simulations are required before a theory can be developed to be included in MOGLI.

While several ingredients are still missing, this work represents a first step for multi-fluid cosmological simulations. These next generation of large-scale simulations would overcome the vexing converging issue in particular in the CGM that current models suffer (see discussion in § 6.2). In contrast – as demonstrated in § 4.2.2 – the total cold gas mass of MOGLI is independent of resolution, and thus can lead to converged large-scale simulations and a robust comparison to observations. To do so, however, it is important to recall that multi-fluid simulations are not as easily interpretable as single-phase ones. For instance, the sub-resolution morphology and kinematics have to be defined as both absorption (Hummels et al. 2017; Singh Bisht et al. 2024; Rudie et al. 2019) as well as emission (e.g. Gronke et al. 2016; Hansen & Oh 2006; Chang & Gronke 2024) crucially depends on them. While some results (such as the clump mass distribution; Gronke et al. 2022; Tan & Fielding 2023) are already known, and more small-scale simulations are needed to parametrize this information. This information can then be used to alter tools such as Trident (Hummels et al. 2017) to make them aware of the subgrid details in a multi-fluid simulation.

7 CONCLUSIONS

In this study, we introduce our new MOGLI subgrid model to account for the subgrid cold gas behaviour, using multifluid hydrodynamics. We use the theoretical framework developed and confirmed in previous work (Fielding et al. 2020; Tan et al. 2021; Gronke et al. 2022; Das & Gronke 2024), and the multifluid implementation (Weinberger & Hernquist 2023) in AREPO (Springel 2010; Weinberger et al. 2020). First, we present the details of our models which consists of,

- Mass, momentum and energy fluxes (\dot{Q}), from drag forces (\dot{Q}_{drag}), turbulent mixing (\dot{Q}_{mix}), and cold gas growth (\dot{Q}_{grow}).
- A local turbulent velocity estimation methods (v_{turb}) based on a Kolmogorov scaling-based method ($v_{\text{turb,ko1}}$), or a velocity gradient-based approach ($v_{\text{turb,grad}}$).
- an estimate of the cold gas surface and cross-sectional area ($2h(\alpha)$ and $A_{\text{cross}}(\alpha)$, respectively).

Second, we separately verify the different parts of the MOGLI model for the two local turbulence estimates. We compare the MOGLI runs with resolved benchmark single-fluid Athena++ simulations for verification. We test the quantities across different turbulent Mach numbers, resolved/unresolved initial cold clouds, resolution and random seeds for turbulent driving, for a robust comparison. The following are the main conclusions from our verification and tests in this study:

- We show that the reduced version of the MOGLI model for non-radiative mixing, i.e. $\dot{Q}_{\text{non-rad}} = \dot{Q}_{\text{drag}} + \dot{Q}_{\text{mix}}$, matches the benchmarks non-radiative Athena++, both qualitatively and quanti-

tatively, in terms of the destruction timescales, across all different parameters, with very similar mean and scatter in $t_{\text{half}}/t_{\text{cc}}$,

- We find that MOGLI model leads to physically consistent interaction between the phases in both resolved and unresolved cold gas structures, where the mass exchange only happens at the interfaces when the cold gas is resolved and throughout the structure when unresolved,
- The full MOGLI model for radiative mixing, shows the expected behaviour of cold gas growth at short cooling timescales and cold gas destruction for long cooling timescales, across all different parameters,
- We verify that the full MOGLI model for radiative mixing, quantitatively matches the expected cold gas mass growth timescales, with very similar mean and scatter in $t_{\text{grow}}/t_{\text{grow,theory}}$ between the benchmark Athena++ runs and MOGLI runs. In both, we find the mean t_{grow} to be $\sim 1.5t_{\text{grow,theory}}$,
- The full MOGLI model for radiative mixing, also recreates the cold gas survival criterion from Gronke et al. (2022), as an emergent process, i.e., while ‘survival’ is not explicitly implemented in MOGLI, it can recover this larger scale result.
- We show that the cold gas dispersion is similar between the full MOGLI model for radiative mixing and analogous benchmark Athena++ runs. The agreement is better in case of a resolved, initial cold gas cloud, compared to the unresolved initial cold gas cloud,
- All the verification tests hold true, regardless of the local turbulent velocity estimation method,
- We demonstrate the strength of the MOGLI model by running a 64^3 cells simulation using MOGLI with 100 unresolved clouds, which would require $\sim 3000^3$ cells in a single-fluid code without a subgrid model.

Our study presents our new physically motivated, multifluid subgrid model MOGLI. We have extensively tested and verified the model across a wide range of possible simulation parameters, to ensure a robust and consistent model. This work will be a useful development towards running converged large-scale simulations with subgrid prescriptions for the unresolved cold gas. However, this MOGLI has many avenues for improvement like the inclusion of the molecular phase, in-situ cold gas formation, subgrid turbulence prescription, etc, which we hope to tackle in future work.

ACKNOWLEDGEMENTS

We thank Aniket Bhagwat, Bo Peng, Drummond Fielding, Matthew Smith, Rajsekhar Mohapatra, Ruediger Pakmor, and Volker Springel for their helpful discussions. HD thanks staff and colleagues at the Max Planck Institute for Astrophysics and The International Max Planck Research School on Astrophysics for their valuable support during the research. MG thanks the Max Planck Society for support through the Max Planck Research Group. RW acknowledges the funding of a Leibniz Junior Research Group (project number J131/2022). Computations were performed on HPC systems Freya and Orion at the Max Planck Computing and Data Facility.

This research made use of AREPO (Springel 2010; Weinberger et al. 2020), Athena++ (Stone et al. 2020), NumPy (Harris et al. 2020), matplotlib (Hunter 2007), SciPy (Virtanen et al. 2020) and inspector-gadget.

DATA AVAILABILITY

Data related to this work will be shared on reasonable request to the corresponding author.

REFERENCES

- Abruzzo M. W., Fielding D. B., Bryan G. L., 2024, *ApJ*, **966**, 181
- Armillotta L., Fraternali F., Marinacci F., 2016, *Monthly Notices of the Royal Astronomical Society*, **462**, 4157
- Audit E., Hennebelle P., 2005, *A&A*, **433**, 1
- Bader G., Deuffhard P., 1983, *Numerische Mathematik*, **41**, 373
- Begelman M. C., Fabian A. C., 1990, *MNRAS*, **244**, 26P
- Berczik P., Hensler G., Theis C., Spurzem R., 2003, *Astrophysics and Space Science*, **284**, 865
- Butsky I. S., Fielding D. B., Hayward C. C., Hummels C. B., Quinn T. R., Werk J. K., 2020, *The Astrophysical Journal*, **903**, 77
- Butsky I. S., Hummels C. B., Hopkins P. F., Quinn T. R., Werk J. K., 2024, *MNRAS*, **535**, 1672
- Chandrasekhar S., 1961, *Hydrodynamic and hydromagnetic stability*. Clarendon Press
- Chang S.-J., Gronke M., 2024, *MNRAS*, **532**, 3526
- Chen Z., Oh S. P., 2024, *Monthly Notices of the Royal Astronomical Society*, **530**, 4032
- Chen H.-W., et al., 2023, *ApJ*, **955**, L25
- Choudhury P. P., Sharma P., Quataert E., 2019, *Monthly Notices of the Royal Astronomical Society*, **488**, 3195
- Cox D. P., 2005, *ARA&A*, **43**, 337
- Crighton N. H. M., Hennawi J. F., Simcoe R. A., Cooksey K. L., Murphy M. T., Fumagalli M., Prochaska J. X., Shanks T., 2015, *Monthly Notices of the Royal Astronomical Society*, **446**, 18
- Das H. K., Gronke M., 2024, *MNRAS*, **527**, 991
- Das H. K., Choudhury P. P., Sharma P., 2021, *Monthly Notices of the Royal Astronomical Society*, **502**, 4935
- Donahue M., Voit G. M., 2022, *Phys. Rep.*, **973**, 1
- Eswaran V., Pope S., 1988, *Computers & Fluids*, **16**, 257
- Farber R. J., Gronke M., 2021, *arXiv e-prints*, **17**, 1
- Faucher-Giguère C.-A., Oh S. P., 2023, *ARA&A*, **61**, 131
- Federrath C., Klessen R. S., 2012, *ApJ*, **761**, 156
- Field G. B., Field G. B., 1965, *The Astrophysical Journal*, pp 531–567
- Fielding D. B., Ostriker E. C., Bryan G. L., Jermyn A. S., 2020, *The Astrophysical Journal*, **894**, L24
- Gronke M., Peng Oh S., 2018, *Monthly Notices of the Royal Astronomical Society: Letters*, **480**, L111
- Gronke M., Dijkstra M., McCourt M., Oh S. P., 2016, *ApJ*, **833**, L26
- Gronke M., Oh S. P., Ji S., Norman C., 2022, *MNRAS*, **511**, 859
- Hansen M., Oh S. P., 2006, *MNRAS*, **367**, 979
- Harfst S., Theis C., Hensler G., 2004, *Publications of the Astronomical Society of Australia*, **21**, 228
- Harris C. R., et al., 2020, *Nature*, **585**, 357
- Heckman T. M., Thompson T. A., 2017, *arXiv e-prints*, p. arXiv:1701.09062
- Hidalgo-Pineda F., Farber R. J., Gronke M., 2024, *MNRAS*, **527**, 135
- Huang S., Katz N., Scannapieco E., Cottle J., Davé R., Weinberg D. H., Peebles M. S., Brüggem M., 2020, *MNRAS*, **497**, 2586
- Hummels C. B., Smith B. D., Silvia D. W., 2017, *The Astrophysical Journal*, **847**, 59
- Hummels C. B., et al., 2019, *The Astrophysical Journal*, **882**, 156
- Hummels C. B., Rubin K. H. R., Schneider E. E., Fielding D. B., 2024, *ApJ*, **972**, 148
- Hunter J. D., 2007, *Computing in Science & Engineering*, **9**, 90
- Ji S., Oh S. P., Masterson P., 2019, *Monthly Notices of the Royal Astronomical Society*, **487**, 737
- Kanjilal V., Dutta A., Sharma P., 2021, *Monthly Notices of the Royal Astronomical Society*, **501**, 1143
- Kannan R., Garaldi E., Smith A., Pakmor R., Springel V., Vogelsberger M., Hernquist L., 2022, *Monthly Notices of the Royal Astronomical Society*, **511**, 4005
- Kim C.-G., Ostriker E. C., 2015, *ApJ*, **802**, 99
- Kim C.-G., Ostriker E. C., 2017, *ApJ*, **846**, 133
- Klein R. I., McKee C. F., Colella P., 1994, *ApJ*, **420**, 213
- Lan T.-W., Fukugita M., 2017, *ApJ*, **850**, 156
- Ledos N., Takasao S., Nagamine K., 2024, *MNRAS*, **527**, 11304
- Levinson F. H., Roberts W. W. J., 1981, *ApJ*, **245**, 465
- Lorensen W. E., Cline H. E., 1987, in *Proceedings of the 14th Annual Conference on Computer Graphics and Interactive Techniques. SIGGRAPH '87*. Association for Computing Machinery, New York, NY, USA, p. 163–169, doi:10.1145/37401.37422, <https://doi.org/10.1145/37401.37422>
- Mandelker N., Nagai D., Aung H., Dekel A., Birnboim Y., van den Bosch F. C., 2020, *Monthly Notices of the Royal Astronomical Society*, **494**, 2641
- Martizzi D., Fielding D., Faucher-Giguère C.-A., Quataert E., 2016, *MNRAS*, **459**, 2311
- McCourt M., Oh S. P., O’Leary R., Madigan A.-M., 2018, *Monthly Notices of the Royal Astronomical Society*, **473**, 5407
- McKee C. F., Ostriker J. P., 1977, *The Astrophysical Journal*, **218**, 148
- Mccourt M., Sharma P., Quataert E., Parrish I. J., 2012, *Monthly Notices of the Royal Astronomical Society*, **419**, 3319
- Mohapatra R., Federrath C., Sharma P., 2020, *Monthly Notices of the Royal Astronomical Society*, **493**, 5838
- Mohapatra R., Jetty M., Sharma P., Federrath C., 2022, *Monthly Notices of the Royal Astronomical Society*, **510**, 3778
- Naab T., Ostriker J. P., 2017, *ARA&A*, **55**, 59
- Okamoto T., Eke V. R., Frenk C. S., Jenkins A., 2005, *MNRAS*, **363**, 1299
- Oppenheimer B. D., Davé R., 2006, *MNRAS*, **373**, 1265
- Pakmor R., Springel V., Bauer A., Mocz P., Muñoz D. J., Ohlmann S. T., Schaal K., Zhu C., 2016, *MNRAS*, **455**, 1134
- Pedregosa F., et al., 2011, *Journal of Machine Learning Research*, **12**, 2825
- Peebles M. S., et al., 2019, *ApJ*, **873**, 129
- Péroux C., Howk J. C., 2020, *Annual Review of Astronomy and Astrophysics*, **58**, 363
- Prosperetti A., Tryggvason G., 2007, *Computational Methods for Multiphase Flow*. Cambridge University Press
- Ramesh R., Nelson D., 2024, *MNRAS*, **528**, 3320
- Rauch M., Sargent W. L. W., Barlow T. A., 1999, *ApJ*, **515**, 500
- Rosdahl J., Schaye J., Dubois Y., Kimm T., Teyssier R., 2017, *MNRAS*, **466**, 11
- Rudie G. C., Steidel C. C., Pettini M., Trainor R. F., Strom A. L., Hummels C. B., Reddy N. A., Shapley A. E., 2019, *ApJ*, **885**, 61
- Saurel R., Abgrall R., 1999, *Journal of Computational Physics*, **150**, 425
- Scannapieco E., Brüggem M., 2008, *ApJ*, **686**, 927
- Scannapieco C., Tissera P. B., White S. D., Springel V., 2006, *Monthly Notices of the Royal Astronomical Society*, **371**, 1125
- Schaye J., Carswell R. F., Kim T.-S., 2007, *MNRAS*, **379**, 1169
- Schmidt W., Federrath C., 2011, *A&A*, **528**, A106
- Schmidt W., Niemeyer J. C., Hillebrandt W., 2006, *A&A*, **450**, 265
- Semelin B., Combes F., 2002, *Astronomy & Astrophysics*, **388**, 826
- Semenov V. A., 2024, *arXiv e-prints*, p. arXiv:2410.23339
- Sharma P., Parrish I. J., Quataert E., 2010, *Astrophysical Journal*, **720**, 652
- Sharma P., McCourt M., Quataert E., Parrish I. J., 2012, *Monthly Notices of the Royal Astronomical Society*, **420**, 3174
- Singh Bisht M., Sharma P., Dutta A., Nath B. B., 2024, *arXiv e-prints*, p. arXiv:2411.17173
- Smith M. C., Sijacki D., Shen S., 2018, *MNRAS*, **478**, 302
- Smith M. C., Fielding D. B., Bryan G. L., Bennett J. S., Kim C.-G., Ostriker E. C., Somerville R. S., 2024, *arXiv e-prints*, p. arXiv:2408.15321
- Sobacchi E., Sormani M. C., 2019, *Monthly Notices of the Royal Astronomical Society*, **486**, 205
- Springel V., 2010, *MNRAS*, **401**, 791
- Springel V., Hernquist L., 2003, *MNRAS*, **339**, 289
- Stone J. M., Tomida K., White C. J., Felker K. G., 2020, *The Astrophysical Journal Supplement Series*, **249**, 4
- Tan B., Fielding D. B., 2023, *MNRAS*, **000**, 1
- Tan B., Oh S. P., Gronke M., 2021, *Monthly Notices of the Royal Astronomical Society*, **502**, 3179

- Tan B., Oh S. P., Gronke M., 2023, *MNRAS*, **520**, 2571
Townsend R. H. D., 2009, *ApJS*, **181**, 391
Tumlinson J., Peebles M. S., Werk J. K., 2017, *Annual Review of Astronomy and Astrophysics*, **AA**, 1
Veilleux S., Cecil G., Bland-Hawthorn J., 2005, *Annual Review of Astronomy and Astrophysics*, **43**, 769
Veilleux S., Maiolino R., Bolatto A. D., Aalto S., 2020, *A&ARv*, **28**, 2
Virtanen P., et al., 2020, *Nature Methods*, **17**, 261
Walch S., et al., 2015, *MNRAS*, **454**, 238
Wang C., Oh S. P., Ruszkowski M., 2023, *MNRAS*, **519**, 4408
Weinberger R., Hernquist L., 2023, *MNRAS*, **519**, 3011
Weinberger R., Springel V., Pakmor R., 2020, *ApJS*, **248**, 32
Wiersma R. P. C., Schaye J., Smith B. D., 2009, *MNRAS*, **393**, 99
van de Voort F., Bieri R., Pakmor R., Gómez F. A., Grand R. J. J., Marinacci F., 2021, *Monthly Notices of the Royal Astronomical Society*, **501**, 4888

APPENDIX A: LOCAL TURBULENCE ESTIMATION IN 2D

We can generalise the expression for 2D geometries. In 2D, the limits of the integral are different, along with a different definition of the cell volume, leading to a slight variation in Eq. (27),

$$v_{\text{turb,grad,2D}} = (\sigma_{v_x}^2 + \sigma_{v_y}^2)^{1/2} = V_{\text{cell}}^{1/2} \sqrt{\frac{1}{\xi_{2D}} \sum_{i,j}^2 \left(\frac{\partial v_j}{\partial x_i} \right)^2} \quad (\text{A1})$$

where, $\xi_{2D} = 4$.

During our non-radiative turbulent mixing tests, explained later in Sec. 5, we find a $\xi_{3D} = 2$ works better in matching with the benchmark Athena++ simulations. Hence, we use a $\xi_{3D} = 2$ in MOGLI runs. We can also combine both Eq. (27) & (A1) into a single expression for D dimensions,

$$v_{\text{turb,grad,D}} = V_{\text{cell}}^{1/D} \sqrt{\frac{1}{\xi_D} \sum_{i,j}^D \left(\frac{\partial v_j}{\partial x_i} \right)^2}$$

where, $\xi_D = \begin{cases} 4 & \text{if } D = 2 \\ 3 & \text{if } D = 3 \text{ Analytical} \\ 2 & \text{if } D = 3 \text{ MOGLI} \end{cases} \quad (\text{A2})$

This paper has been typeset from a $\text{\TeX}/\text{\LaTeX}$ file prepared by the author.